NTNU – Trondheim
Norwegian University of
Science and Technology

Gravity Wave Climatology for Trondheim using a Meteor Radar.

Nils Henrik Kolnes

Master of Science in Physics and Mathematics
Submission date: June 2013
Supervisor: Robert Edward Hibbins, IFY

Norwegian University of Science and Technology
Department of Physics

Gravity Wave Climatology for Trondheim (64,4^{o}N, 10,5^{o}E) using a Meteor Radar.

Nils Henrik Kolnes
Department of physics, NTNU, N-7491 Trondheim, Norway

Academic supervisor: Robert E. Hibbins

June 20, 2013

Abstract

In this thesis, a gravity wave climatology for the altitude range of the airglow (hydroxyl) layer of 83 to 91km have been made using data from a meteor radar located at Dragvoll (64,4^{o}N, 10,5^{o}E) in Trondheim. The climatology stretches from the 9th of September until the 30th of April.

The wave "activity" results, from the average daily variance in the perturbed line of sight velocity, show two minima at the equinoxes and a maxima between them in mid winters. The results agree with similar studies from Rothera (68^{o}S) and Esrange (68^{o}N) which is comparable with Trondheim in latitude.

A case study is made for the 3rd of December comparing wave propagation directions shown in airglow images with hourly direction plots from the meteor radar. The comparison shows agreement between the two methods proving that meteor radars can be used to study preferred wave propagation directions.

Monthly averaged preferred wave propagation direction results for the period 9th of September 2012 to the 30th of April 2013, show equatorward preferred wave propagation direcion during fall, abruptly changing through end of fall to strictly polewards in November. End of winter through start of spring shows an equatorwards and westwards preferred wave direction rotating counter clockwise to equatorwards and eastwards. The results were comparable with climatologies made with airglow imagers due to the chosen altitude range. Comparisons showed both agreement and disagreement in preferred wave propagation direction.

Sammendrag på norsk

Denne oppgaven presenterer en gravitasjonsbølge klimatologi laget med data fra en meteor-radar som stå r på Dragvoll (64,4^{o}N, 10,5^{o}E) i Trondheim. Høyeden dataen er samlet inn fra er 83 til 91 km, som er samme høyde hydroxyl-laget i atmospfæren ligger. Klimatologien går fra 9. september 2012 til 30. april 2013.

Resultatene for bølgeaktivitet, målt fra variansen i perturbert vindhastiget, viser minimums punkter ved vår- og høstjevndøgn samt et maksimumspunkt midt vinters. Resultatene stemmer overens med lignende studier gjort ved Rothera (68^{o}S) og Esrange (68^{o}N), som begge er sammenlignbare med Trondheim på breddegrad.

For 3. desember er data som viser gravitajonsbølger, fra et infrarødt kamera som måler stråling fra hydroxyl-laget("airglow imagers"), sammenlignet med "retningsplot" for samme tidsperiode. "Retningsplot" viser den foretrukne bølgeretningen time for time. Resultatene stemmer overens og viser at data fra en meteor radar kan blir brukt til å bestemme gravitasjonsbølgers foretrukne propageringsretning.

De månedlige gjennomsnittlige foretrukket bølge propagerings retnings resultatene, for perioden 9. september 2012 til 30. april 2013, viser sørlig foretrukket propagerings retning gjennom høsten. Retningen endres raskt i slutten av høsten slik at i starten av vinteren er den rett nord. Fra slutten av vinter til start av vår roterer foretrukket propagerings retning fra sør-vest, mot klokka, til sør-øst. Resultaten ble sammenlignet med klimatologier laget med "airglow imagers" og viste overensstemmelse med en andel av klimatologiene.

Acknowledgements

I would like thank my supervisor Robert E. Hibbins for his support and guidance through out this thesis. It is always inspiring and motivating discussing my results with him. I would also like to thank him and my mother Kirsti Veggeland for correcting my English.

Contents

List of Figures

Chapter 1

Introduction

Atmospheric gravity waves can be observed as striped patterns in the clouds, or felt in an aeroplane when the ride gets bumpy. They have been a studied phenomena for many years and many of their secrets have been uncovered.

What has yet to be fully understood is how gravity waves behave in the mesosphere. This is because the mesosphere is an elusive part of the atmosphere, its density is too low for aeroplanes to fly there and too high for satellites to orbit in.

Gravity waves carries energy from the lower parts of the atmosphere, up to the middle and upper parts. It is believed that gravity waves deposit most of their energy in the mesosphere. The deposited energy drives some of the large circulations in the upper atmosphere, which again affects the middle and lower atmosphere's wind systems. Studying gravity waves in the mesosphere could therefore result in better understanding of the atmosphere as a whole.

Over the years, several ground based methods for studying gravity waves have been developed. In this thesis, a SKiYMET meteor radar is used. The meteor radar measures the movement and position of ionized air trails left by thousands of meteors burning up in the upper atmosphere. Data from the 9th of September 2012 until the 30th of April 2013 will be used to create a gravity wave climatology for Trondheim. The climatology is generated in a manner such that it can be directly compared with similar studies using an ariglow imager, to check the validity of the meteor radar.

Chapter 2

Theory

2.1 The atmosphere

The atmosphere is divided into several layers as seen in figure(2.1). At the bottom is the troposphere, which is where most of the observable weather phenomena occur. Above the troposphere is the stratosphere where the ozone layer is found. The mesosphere and lower thermosphere are called the MLT region and lay on top of the Stratosphere. In this region the periodical waves of the atmosphere dissipate and deposit their momentum. The different wave types are planetary waves, solar atmospheric tides and gravity waves. These waves propagate upwards through the atmosphere connecting the different layers through momentum and temperature.

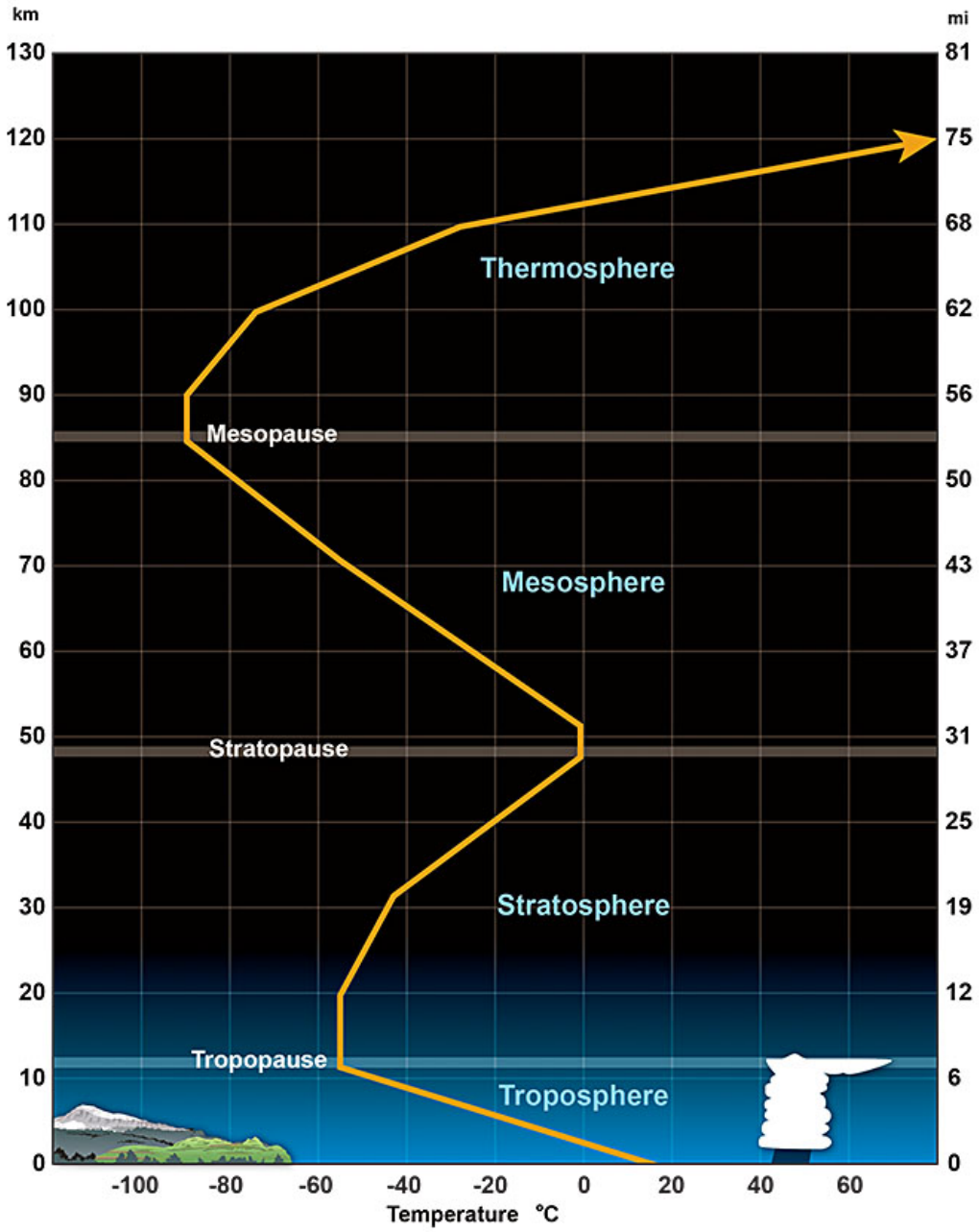

Figure 2.1:
Illustration of the height and temperature profile of the atmosphere. [16]

2.1.1 Gravity waves

Gravity waves are created when a parcel of air is moved upwards to a height where the surrounding density is lower. Gravity will act on the parcel, forcing it back to equilibrium. The gained speed from the gravitational pull will make the parcel overshoot its equilibrium and therefore end up in a place where the surrounding density is higher. Buoyancy forces the wave upwards again, and an oscillation has begun. Gravity waves are also called Buoyancy waves. They follow the same concept as water waves, but instead of having a discreet step in density from water to air, the density decreases continuously with height.

A gravity wave can be visualized by imagining a corrugated sheet moving through a fluid, figure(2.2) illustrates this.

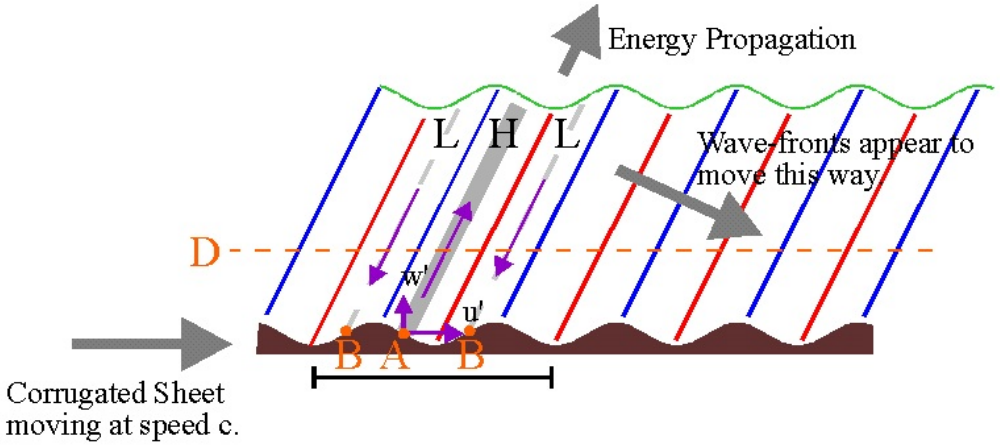

Figure 2.2:
Illustration of the physical picture of a gravity wave. [5]

The sheet is moving towards the right with speed C. At point "A" the air gets forced vertically by the "w'-" component and horizontally by the "u'-" component. The resulting propagation direction is shown by the diagonal purple arrow. By forcing the air upwards, a high pressure region will be made, illustrated by the thick grey line. At point "B" the opposite will occur. The corrugation sheet will appear to be falling away, forcing the air in this region to fall. Pulling the air towards the sheet will generate a low pressure region, illustrated by the thin broken grey lines.

The red and blue lines illustrate where the air is hottest and coldest. Adiabatic processes make the lowest part of the waves warmest and the highest parts coldest.

The propagation direction of the gravity waves appears to be slightly downwards towards the right, but since the sheet in point "A" is forcing air up and to the right, this becomes the direction of propagation for the energy. When an air parcel gets forced upwards, the air parcel above will also be forced upwards, and the one above, and so on.

When propagating vertically the amplitude of the gravity wave increases with height. Energy is conserved and from equation(2.1) it is clear that the oscillation amplitude increases as the density decreases

$$E_k(h) = \frac{1}{2}\rho(h)v(h)^2 \tag{2.1}$$

whereρ is the density and h is the height.

When gravity waves reach a certain height, they break due to the amplitude getting too large. The critical height is typically somewhere in the MLT. When a wave breaks, it deposits its momentum, meaning that gravity waves act as a momentum transporter from the lower and middle parts of the atmosphere into the mesosphere.

The deposited momentum drives the meridional circulation in the mesosphere. This circulation propagate downwards again, affecting the middle atmosphere. Studying gravity waves in the mesosphere is therefore very important in order to understand processes in other parts of the atmosphere.

Collecting proper data from the mesosphere is hard because the air density is too high for satellites to orbit in, but too low for air planes to travel in. Two ground based methods for observing gravity waves in the MLT will be described in the next chapter.

2.1.2 Tides in the mesosphere

In this thesis the semi diurnal tide will be encountered as a background wind that needs to be removed from the data. It is therefore necessary to understand how it behaves.

The earth rotates at a diurnal cycle. Any point in the atmosphere is therefore subject to diurnal cycled solar radiation (a forcing). If the radiation

is absorbed and then released as heat, the solar heating will have the same cycle as the forcing. The radiation can either be absorbed by ozone in the stratosphere or by water vapour in the troposphere. The heat distribution (the response) $J(t)$ can be written as a Fourier decomposition, done by Jeffery M. Forbes[18] shown in equation(3.1)

$$J(t) = \sum_{n=0}^{N} A_n(\theta, z, \lambda) cos(n\Omega t - \phi_n(\theta, z)) \tag{2.2}$$

where $\Omega = \frac{2\pi}{24}$ and t is in hours. The different terms of equation(3.1) ($n = 1, 2, 3...$) is the diurnal-, semidiurnal-, terdiurnal tide and so on. Generally it is the diurnal component that is the largest, but at higher latitudes (like Trondheim) the semidiurnal component dominates. The reason is the seasonal changes in the solar radiation cycle.

The amplitude of the tides in the mesosphere is also season dependent. Seasonal winds and waves in the lower parts of the atmosphere affect the tides as they propagate up towards the mesosphere.

Chapter 3

Instruments

3.1 Airglow imaging of gravity waves

The hydroxyl radical (OH) is produced naturally in the atmosphere during night time by the following reaction:

$$H + O_3 \rightarrow OH^* + O_2 \tag{3.1}$$

where only the highest vibrational levels of OH^* are produced. Hydroxyl in lower vibrational levels are produced by collisional quenching or cascading. When the molecules cascade through lower levels, light in the infrared and near-infrared region is produced. This is the strongest source of light in the sky during the night.

At the mesopause, about 87 km in altitude, lies a hydroxyl emission layer with a thickness of about 8 km. When gravity waves propagate through this layer they can be seen with an airglow imager, as shown in figure(3.1).

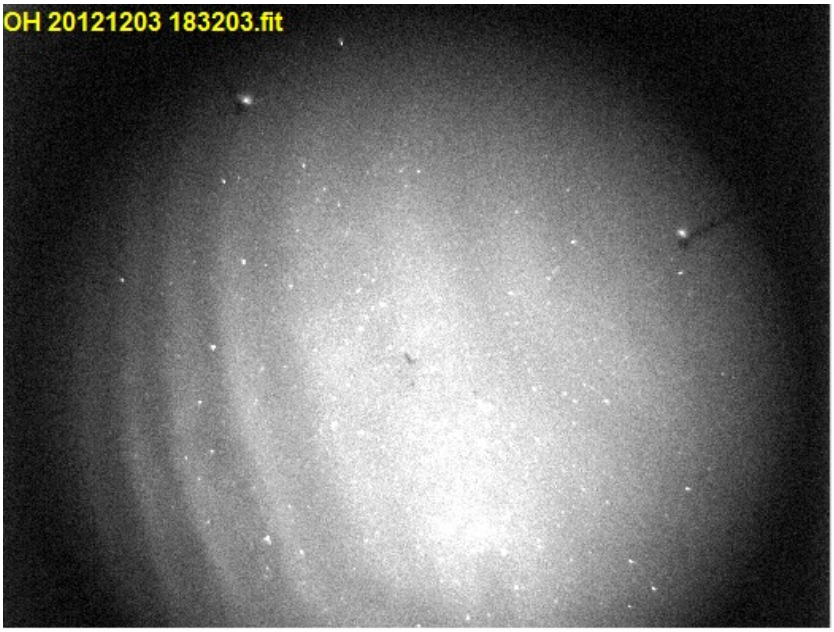

Figure 3.1:
Example picture from the airglow imager at Dragvoll Trondheim. The image is taken 3rd of December 18:32:03.

The airglow imaging technique was, for a long time, the only method for visualizing gravity waves. By measuring multiple images closely spaced in time (to avoid aliasing), the relative amplitude and propagation direction of the gravity wave can be directly observed.

Propagation direction can also be determined by inspecting just one image. Figure(3.1) shows a gravity wave propagating towards the bottom left (in the image). The waves appear strongest in the direction they are propagating. This is because gravity waves have tilted phase fronts. On the upper right part of figure(3.1) the phase fronts are almost perpendicular to the line of sight, meaning the fluctuation in the airglow layer can not be seen. Moving upwards in the image, the phase fronts get more and more parallel with the line of sight, and the perturbations in the hydroxyl layer can be observed.

There is however disadvantages in using an airglow imager when trying to do a climatology of gravity waves. First, they can only be used at night, making it impossible to get continuous data for more than twelve to fourteen hours at a time (depending on latitude and season). An airglow imager also doesn't work if it's cloudy, adding a randomness to any time series of data.

In this thesis, case studies will compare results from the meteor radar with days when gravity waves are observed with airglow imager located at the same place as the radar.

3.2 The SKiYMET meteor radar

The meteor radar used in this thesis is a SKiYMET radar located at Dragvoll in Trondheim (64,4^{o}N, 10,5^{o}E). The radar consists of eight transmitting antennas and five receiving antennas as shown in figure(3.2). Transmitting antennas sample at about 1 kHz. Sampling signal has a set frequency of $34,21$ MHz and a wave length (λ) of about 9 m.

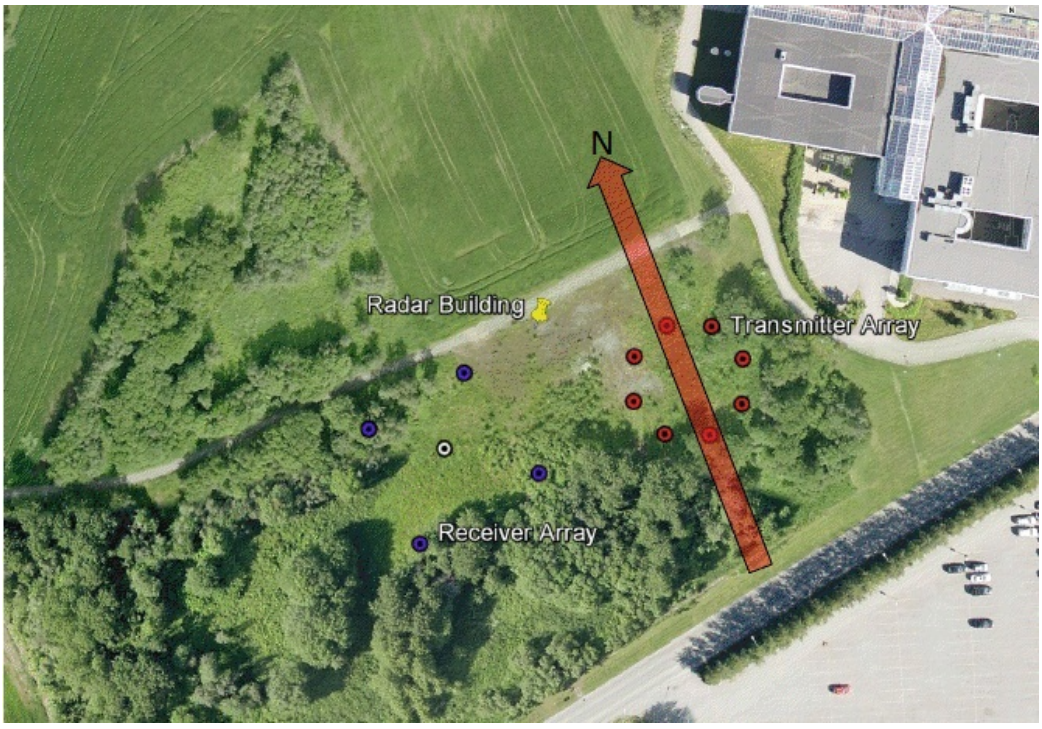

Figure 3.2:
Set up of the meteor radar.

The transmitters are set up in an octagon, displaced by λ from its nearest neighbours. They are set to focus the majority of the transmitted power into a zenith angle between 20° and 50°. The set up also causes destructive

interference for every 45° azimuthal angle (0° being strictly eastwards) and constructive interference in between. See figures (3.3) and (4.2).

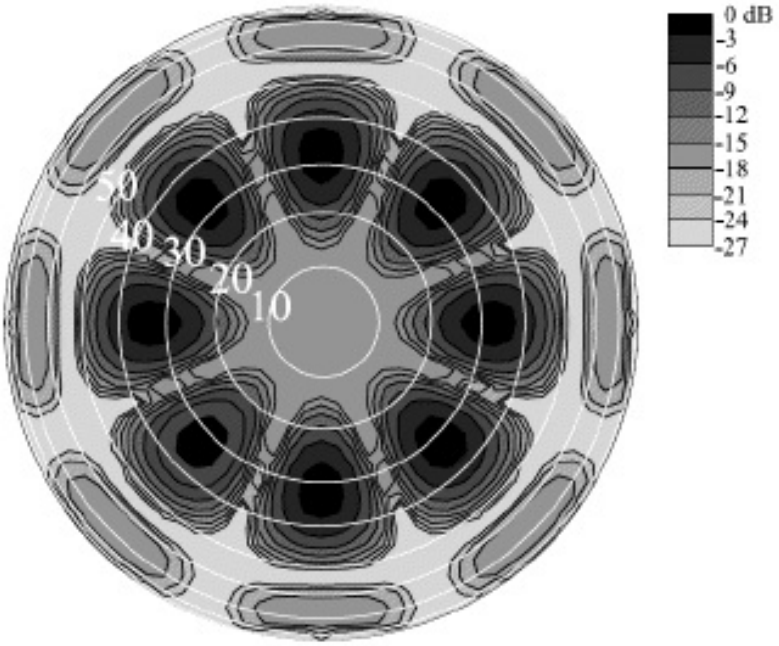

Figure 3.3:
Distribution of the radiated power of the radar in dB. [14]

The Receivers are set up in a cross with the fifth antenna in the center. Two receivers are placed $2,5\lambda$ from the center receiver while the other two, 2λ (see figure(3.2)). This set up makes it possible for the radar to determine where on the sky a detection is made. By comparing phase differences on the two receiving antenna pairs, the software predicts several positions (in azimuthal and zenith angle) for each meteor. The position with the lowest error is chosen as the correct position, given that the lowest error is below a certain value. If two or more positions obtain the same lowest error, then the meteor is reported as ambiguous. In this thesis all meteors with ambiguity > 1 are ignored.

A meteor radar measures ionised trails created by meteors burning up in the upper atmosphere. The trails last for up to four seconds in which they drift with the winds. Since the meteor is sampling at 1 kHz it measures lots

of positions as the trail its moving. From these position readings the meteor radar measures the line of sight velocity of the meteor trail hence also the line of sight velocity of the wind.

Meteors burn up at different heights. In this thesis (83 - 91) km is the height interval of interest. This is where the airglow layer is; see section(3.1).

Meteors are detected at all times. The meteor detection frequency is highest in the morning, and lowest in the evening,(see the "(a) Meteor Flux" plot in figure(4.1)). The reason is that the earth rotates around its own axis as well as around the sun. In the morning the radar is tilted in the same direction as the orbital velocity of the earth. Since meteors are particles or bodies in space that collide with the earth, the flux of meteors is bigger when the radar is tilted in the direction of earth's orbital velocity. It is the same concept as blowing dusty air through a filter. The dust will gather on the surface that faces the air velocity.

The number of meteors detected in 24 hours is on average about 15000, but varies on a daily basis. Meteor showers for example, can give a lot of data one day, but the variation also depends on the season. For example in autumn, on the northern hemisphere the earth's axis is tilted towards the orbital velocity of the earth, which causes an increase in meteor flux. The density of meteors in earth's orbit is not constant which also affects the seasonal change in meteor flux. Figure(3.4) shows the daily meteor count rated from a similar meteor radars located at Juliusruh (54^0N) and Andenes ((69^0N)) between November 1999 and April 2004. From figure(3.4) it can be seen that there are most meteors during summer and least during winter.

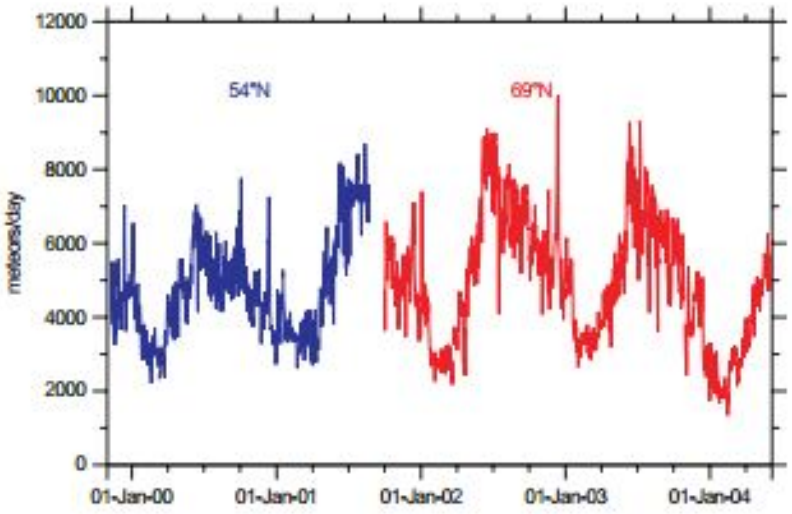

Figure 3.4:
The seasonal changes in meteors detected per day. [8]

The data files recorded by the radar contain several parameters. Each parameter with a short description is shown in figure(3.5).

Data Field	Description
Date	The date of the detection CCYY/MM/DD relative to UTC.
Time	The time of the detection HH:MM:SS.XYZ in UTC where XYZ is the millisecond of the detection. (Note that this represents the relative accuracy of the detection, not the absolute accuracy which, in the normal mode of operation, is +/- 1 second).
File	The file name extension used to store the raw data for this detection (VWXYZ characters from [0..9, A..Z]).
Rge	The range of the detection in km to one decimal place (WXY.Z).
Ht	The corrected height above ground of the detection in km (WXY.Z).
Vrad	The radial drift velocity of the trail in m/s (WX.YZ).
DelVr	The standard deviation of the radial velocity measurement obtained from the 5 antenna pairs in the interferometer. Note that the analysis rejects data with delVr > 5.5 m/s so that this represents a limiting value for this field in the MPD file.
Theta	The zenith angle of the detection in degrees (XY.Z).
Phi0	The azimuth angle of the detection in degrees measured anticlockwise from East (WXY.Z).
Ambig	The number of locations this detection could have originated from (X).
Delphase	The worst phase error between antennas if the measured azimuth and zenith of the detection are correct (XY.Z). Measured in degrees.
ant-pair	The antenna pair with the worst phase error (XY).
IREX	The receive channel used in the analysis for certain single-channel data quality tests. This is always "1" during normal operation.
amax	The peak value of the amplitude of the meteor echo in digitiser units. This may be greater than 32767 if channel saturation has occurred (VWXYZ).
Tau	The decay time of the meteor in seconds. This is a half-life, *not* a 1/e time constant (.XYZ).
vmet	The entrance speed of the meteor in km/s. Bad values are characterised with "-9.99" (WX.YZ).
snrdb	The signal-to-noise ratio for this meteor (X.YZ).

Figure 3.5:
Parameters measured by the meteor radar.[9]

A meteor data file is shown in figure(3.6).

Date	Time	File	Rge	Ht	Vrad	delVr	Theta	Phi0	Ambig	Delphase	ant pair	IREX	amax	Tau	vmet	snrdb
2012/09/10	0:00:03.546	00000	98.0	91.7	24.37	1.66	20.8	154.8	1	15.9	25	1	1842.	.057	-9.99	12.0
2012/09/10	0:00:13.570	00001	116.0	92.6	27.21	1.42	37.3	187.9	1	8.3	41	1	2147.	.042	-9.99	12.8
2012/09/10	0:00:13.622	00002	264.2	86.5	57.80	.46	72.0	198.5	1	15.9	53	1	2174.	.043	-9.99	15.1
2012/09/10	0:00:13.713	00003	254.2	83.9	45.70	3.13	71.8	171.2	1	21.7	52	1	954.	.047	-9.99	7.1
2012/09/10	0:00:17.730	00004	192.2	94.9	-45.32	.06	61.2	260.5	1	10.8	45	1	7834.	.076	-9.99	24.6
2012/09/10	0:00:18.737	00005	130.0	98.6	-36.05	1.36	41.0	188.5	1	7.0	15	1	2896.	.024	-9.99	15.2
2012/09/10	0:00:23.209	00006	220.2	92.3	7.05	.60	66.1	322.6	1	10.4	51	1	2687.	.085	-9.99	13.6
2012/09/10	0:00:23.209	00007	102.0	93.8	24.46	.40	23.3	162.5	1	7.8	54	1	4499.	.044	-9.99	18.6
2012/09/10	0:00:23.922	00008	124.0	85.4	21.57	.92	46.9	327.3	1	6.5	24	1	1061.	.205	-9.99	6.9
2012/09/10	0:00:33.561	00009	114.0	96.5	-25.63	.94	32.5	210.1	1	12.1	45	1	3681.	.030	-9.99	16.6
2012/09/10	0:00:39.918	0000A	106.0	85.4	14.96	.82	36.6	283.4	1	4.7	53	1	1430.	.206	-9.99	8.4
2012/09/10	0:00:41.449	0000B	118.0	85.7	-14.55	1.61	43.8	79.2	1	12.2	15	1	1050.	.202	-9.99	6.9
2012/09/10	0:00:43.914	0000C	192.2	98.7	-43.84	.02	59.8	184.7	1	11.1	53	1	6570.	.285	-9.99	22.7
2012/09/10	0:00:48.861	0000D	194.2	92.4	9.24	1.88	62.3	125.6	1	8.5	42	1	1401.	.089	-9.99	9.6
2012/09/10	0:01:02.893	0000E	184.2	99.7	-28.27	3.05	57.9	340.1	1	23.3	42	1	1880.	.025	-9.99	10.7
2012/09/10	0:01:27.425	0000F	378.3	93.4	-78.96	1.23	77.4	149.4	2	23.7	15	1	1045.	.077	-9.99	7.6
2012/09/10	0:01:27.425	0000F	216.2	73.0	-78.96	1.23	71.2	176.1	2	26.5	13	1	1045.	.077	-9.99	7.6
2012/09/10	0:01:33.142	0000G	184.2	83.1	-3.85	2.63	63.9	211.8	1	8.6	15	1	1083.	.143	-9.99	6.8
2012/09/10	0:01:43.165	0000H	98.0	81.0	8.88	.38	34.5	303.1	1	11.3	15	1	1707.	.235	-9.99	9.7
2012/09/10	0:01:45.635	0000I	88.0	77.2	6.35	.29	28.8	335.5	1	7.7	35	1	2755.	.397	-9.99	13.7
2012/09/10	0:01:45.972	0000J	232.2	79.5	-32.59	.48	71.0	76.2	1	8.6	45	1	2119.	.058	-9.99	11.9
2012/09/10	0:01:49.042	0000K	106.0	83.8	6.20	1.43	38.1	109.4	1	18.2	45	1	1057.	.280	-9.99	6.3
2012/09/10	0:01:52.744	0000M	112.0	90.6	34.32	.51	36.3	200.8	1	7.1	15	1	1495.	.222	-9.99	10.6
2012/09/10	0:01:55.459	0000N	108.0	93.7	47.50	.97	30.1	156.5	1	11.8	25	1	2049.	.055	-9.99	12.4
2012/09/10	0:01:59.862	0000O	100.0	89.8	-19.96	2.37	26.3	55.8	1	13.3	25	1	1468.	.079	-9.99	8.8
2012/09/10	0:02:03.961	0000R	98.0	81.8	31.88	.17	33.6	232.1	1	8.1	35	1	6118.	.168	-9.99	21.2
2012/09/10	0:02:04.056	0000S	130.0	92.6	-17.14	.59	45.0	206.5	1	14.4	15	1	1392.	.058	-9.99	8.9

Figure 3.6:
Part of a data file generated by the SKiYMET meteor radar.

Important parameters in this project are *Time*, the time a meteor is recorded, *Ht*, the altitude of the meteor trail, *Rge* the distance from the radar to the meteor in kilometres and *Vrad* the meteor line of sight velocity (which will be explained below). *Theta* and *Phi0* are respectively the meteors azimuth and zenith angles, together with *Rge* they form a spherical coordinate system. *ambig* tells whether or not a meteor is ambiguous, if its value is 1 the recorded meteor is unambiguous, while for 2 or more its ambiguous and the meteors position can not be determined with 100 percent accuracy.

The *Vrad* is the line of sight velocity. It is the component of the meteors velocity that is parallel to the transmitted beam. An illustration is made in figure(3.7a). The coloured arrows show the velocity of different meteor trails, as well as the measured line of the line of sight velocities. In later plots red dots will mean positive line of sight velocity, the ionised trail moving away from the radar, while Blue dots mean negative line of sight velocity and the trail moves towards the radar.

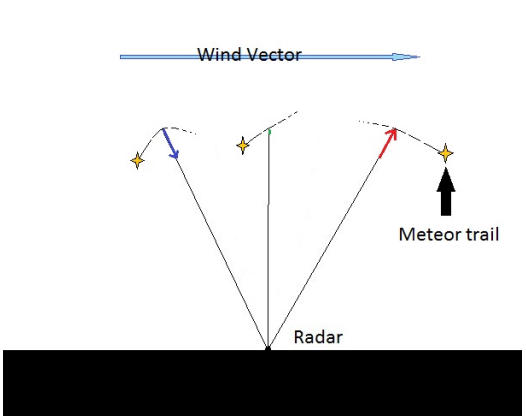

(a) *Meteors burning up in the atmosphere and an illustration of the concept of line of sight velocity*

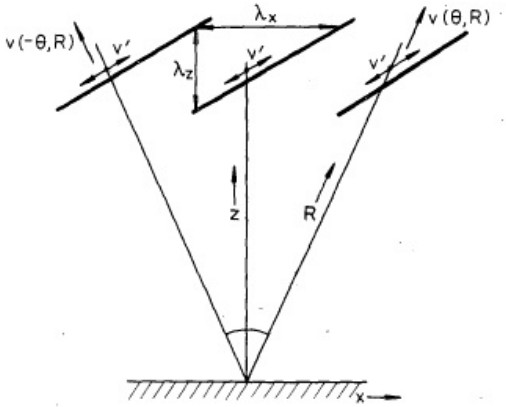

(b) *Illustration of a propagating gravity wave and how variance in line of sight velocity vary with position.* [7]

General concepts of the line of sight velocity

Figure(3.7b) shows a radar in one plane with two transmitting antennas. A gravity wave is passing from left to right. The radar measures the wave in three different locations getting different results for the perturbed line of sight velocity in each measurement. The wave to the left will have a measured perturbed line of sight velocity of ~ 0 since the beam is almost perpendicular to the phase front. The beam measuring the wave to the right will however measure large positive and negative line of sight velocities, since this beam is almost parallel to the phase front. The middle beam measures a line of sight velocity which is somewhere in between the the other two.

Variance in the line of sight velocity

The best way to study gravity waves when using data from a meteor radar, is to look at the variance in the line of sight velocity. When a wave is propagating over the radar as in figure(3.7b), a large variance will be measured in the direction the wave is propagating. The reason is, that as the waves pass over the radar, both the positive and negative line of sight velocities increases due to the tilted phase fronts. If there is no wave activity, the radar only measures a line of sight velocity due to the background wind and the variance will be constant.

Chapter 4

Data analysis

4.1 Meteor radar data

The following plots are generated from data collected by the SKiYMET meteor radar situated at Dragvoll, Trondheim the 10th of September 2012.

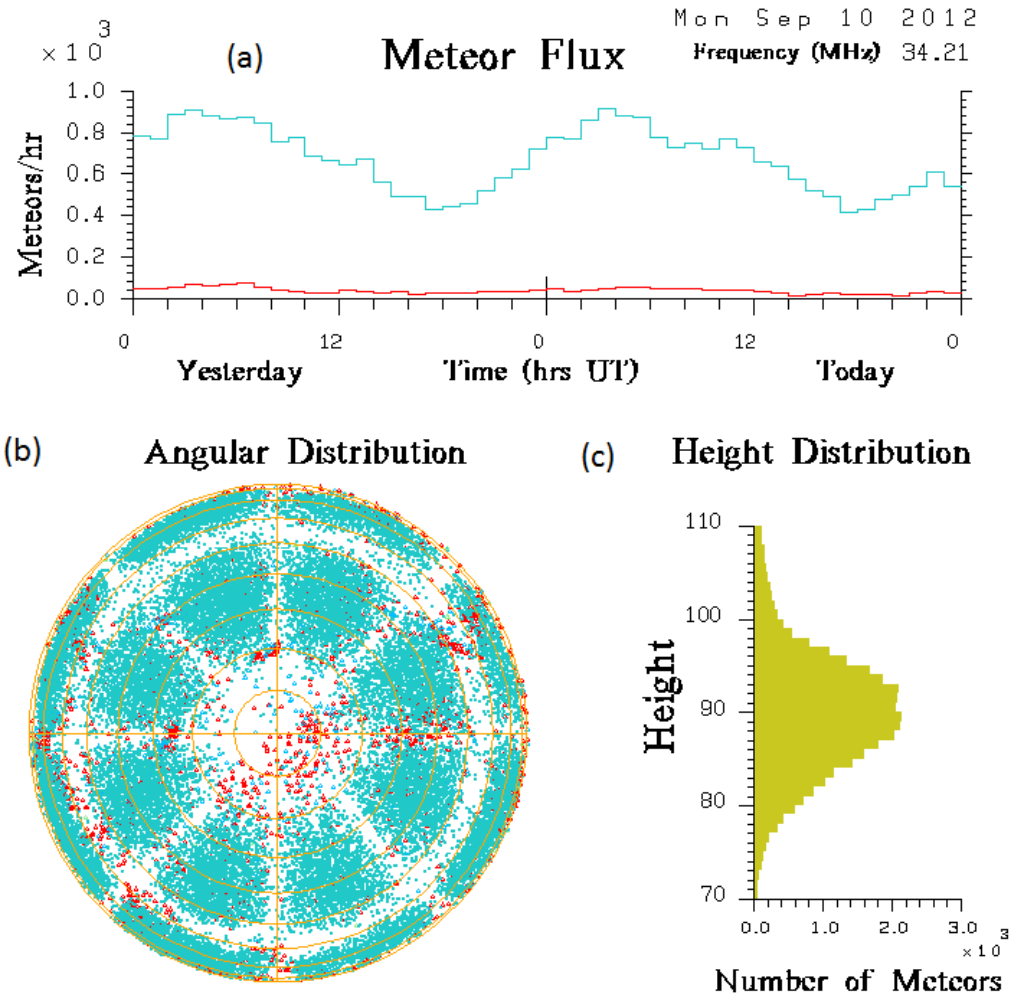

Figure 4.1:
Angular distribution plot, meteor flux graph and height distribution graph from 10th of September 2012, generated by the SKiYMET meteor radar software [10]

Figure(4.1) shows the data that is recorded by the meteor radar. The "Meteor Flux" graph "(a)" displays the diurnal change in meteor flux. The blue line displays the flux of unambiguous meteors, while the red displays the flux of ambiguous meteors."(b)" is the "Angular Distribution" plot which shows how the meteors are distributed over the field of view in spherical coor-

dinates. The red dots represents ambiguous readings the blue unambiguous readings. "Height Distribution", "(c)", shows the meteor density as a function of height. It spikes at $90km$ and is a normal distribution. In this thesis the area of interest will be from $(83-91)km$, as this is symmetric above and below the Hydroxyl layer located at $87km$.

4.1.1 Treating the raw data

The raw data, that the meteor radar receives, needs to be treated before it can be analysed. In this project Matlab R2011a was used to treat the raw data and make the plots. The data files created by the radar is received as a .mpd file, an example of which is presented in figure(3.6). In Matlab, all ambiguous meteor and all meteors not within height range $(83-91)km$ are filtered out. The remaining meteors' positions, in zenith- and azimuthal angle (θ and φ) are converted to cartesian coordinates (x and y) and plotted; Figure (4.2).

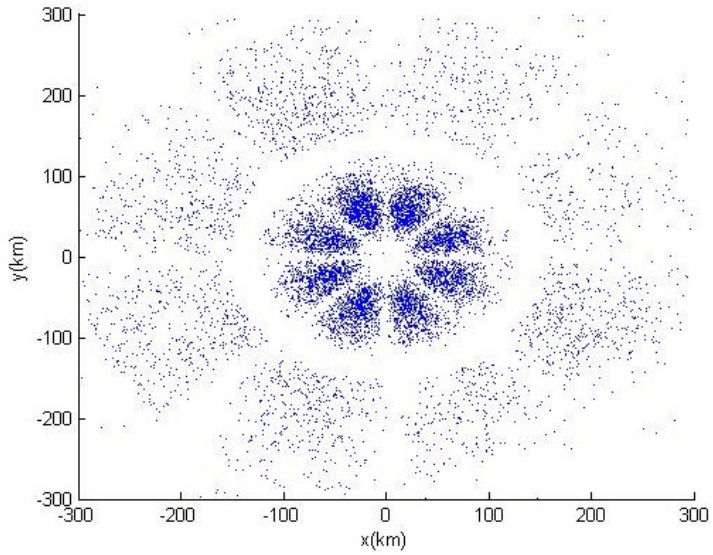

Figure 4.2:
The plot shows all the meteors the SKYiMET radar detected the 10*th of September* 2012*. The x-axis goes from west to east, while the y-axis goes from south to north.* $(0,0)$ *is Zenith above Trondheim.*

Figure(4.2) is similar to the "Angular Distribution" in figure(4.1), but the

coordinate system is changed. The meteors close to the edges are more spread out in the cartesian coordinate system. The reason for changing coordinate system is that a cartesian coordinate system is more suited when visualizing wave activity than a polar coordinate system.

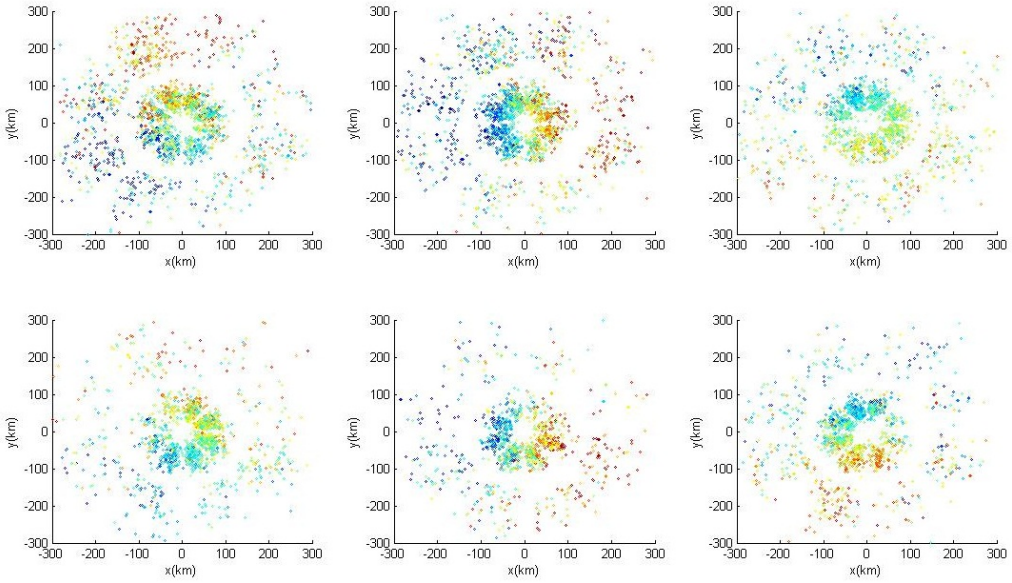

Figure 4.3:
The figure shows all the meteors the SKYiMET radar detected the 10*th of September* 2012 *divided into six fractions with four hours worth of data in each individual sub plot. The colors represent the line of sight velocity of a meteor which goes from* $+70$*(m/s) (red) to* -70*(m/s) (blue). The axis represent the same as in figure(4.2).*

A plot of meteors with their corresponding line of sight velocity is shown in figure(4.3). The data set containg 24 hours of data is divided into six fractions containing four hours of data.

It can be seen from figure(4.3), that there is a uniform line of sight velocity pointing in one direction over the entire field of view. This is the background wind caused primarily by the semi diurnal tide. By inspecting figure(4.3) it is possible to see the twelve hour cyclic behaviour of the semi diurnal tide. The upper and lower plots in figure(4.3) have the same direction of their background wind. Since each plot represents four hours, then plot one through three should be one cycle, which it is.

4.2 Background wind

4.2.1 Making a fitting routine

To be able to measure gravity waves the background wind due to primarily semi diurnal tide has to be removed from the plots. In this thesis a fit was generated to get an estimated value for the zonal ($\vec{U}$) and meridional ($\vec{V}$) component of the background wind.

To make the fit, it was assumed that the background wind was uniform and homogeneous over the entire field of view.

$$f(\varphi, \theta) = (\vec{U}\cos(\varphi)\sin(\theta) + \vec{V}\sin(\varphi)\sin(\theta)) \tag{4.1}$$

Equation(4.1) is the function used to generate the fit. To validate the fit, the $\vec{U}$ and $\vec{V}$ component is plotted for different heights at hourly intervals over an entire day. If the fit is good the plots should agree with the plots generated by the radar.

4.2.2 Testing the fit

Figure(4.4) shows what the estimated fit for the background wind velocity components. Figure(4.5) is a plot generated by the SKiYMET's software for the same time and height intervals as the fit was made for.

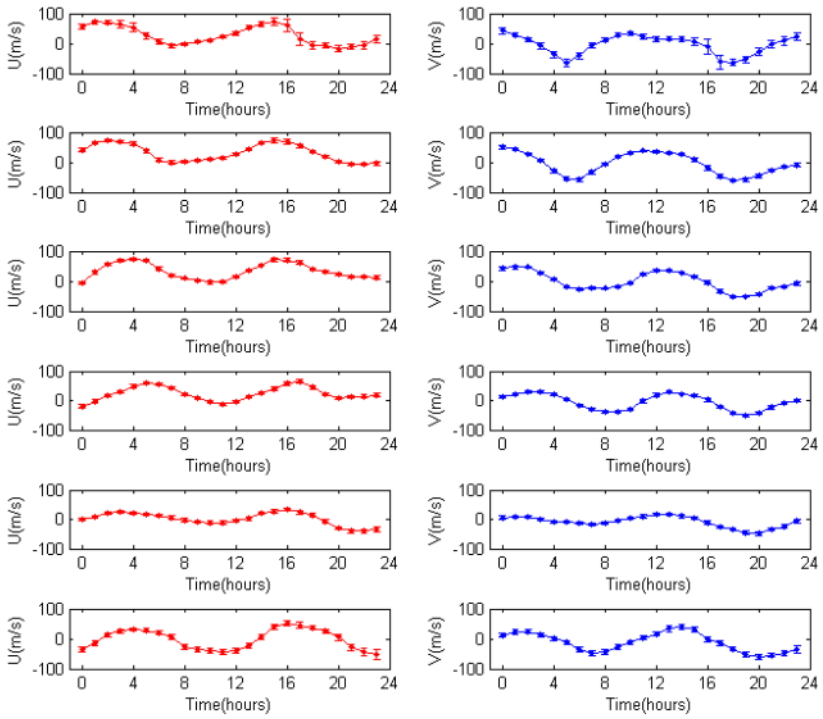

Figure 4.4:
The estimated $\vec{U}$ and $\vec{V}$ plotted every hour for 24 hours for different heights , starting from 82 km at the bottom, increasing stepwise up to 98 km at the two top plots.

By comparing figures(4.4) and (4.5), it is clear that the fit is good. The peaks and troughs occur at the same time and the phase gets slightly shifted backwards as the height increases. The overall shape of the curves also match. Error bars represent a 95 percent confidence interval.

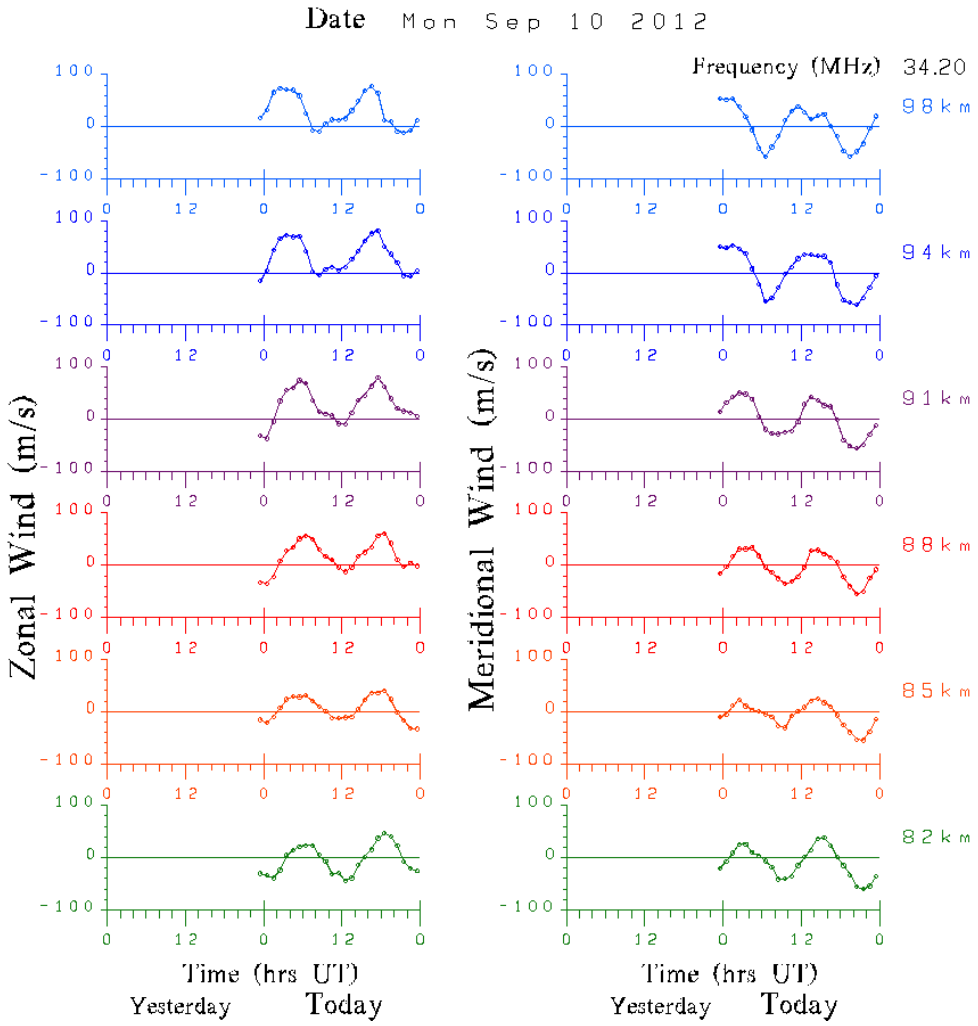

Figure 4.5:
The measured $\vec{U}$ and $\vec{V}$ plotted every hour for 24 hours for different heights , starting from 82 km at the bottom, increasing stepwise up to 98 km at the two top plots.[11]

4.2.3 Removing the background wind

After getting the fitted function it was possible to remove the estimated values for $(\vec{U})$ and $(\vec{V})$ from each meteors line of sight velocity. This was

done using equation(4.2)

$$\Delta LOS = LOS - (\vec{U}\cos(\varphi)\sin(\theta) + \vec{V}\sin(\varphi)\sin(\theta)), \tag{4.2}$$

where θ and φ correspond to the positions of the meteors and ΔLOS is the meteors' perturbed line of sight velocity. To get the best data possible, the parameter θ (the zenith angle) was restricted to (0-60)°. 24 hours worth of data was divided into 23 plots, each fit made with 3 hours of data while only plotting the hour in the middle. Each fit overlaps the previous and the next fit by one hour, meaning the first plot has fitted data from 00:00 until 03:00, while only showing meteors from 01:00 until 02:00. The next plot has a fit made with data from 01:00 to 04:00 and plots the meteors from 02:00 to 03:00. The reason for the fits overlapping was to get as much data as possible to reduce the error in the fitting routine.

The background wind is removed in height intervals of 2 km to reduce the error. The fit converges towards certain values as the intervals get smaller. An interval of 2 km was chosen based on running time of the matlab script as well as making certain there was enough meteors in each interval to get a good fit.

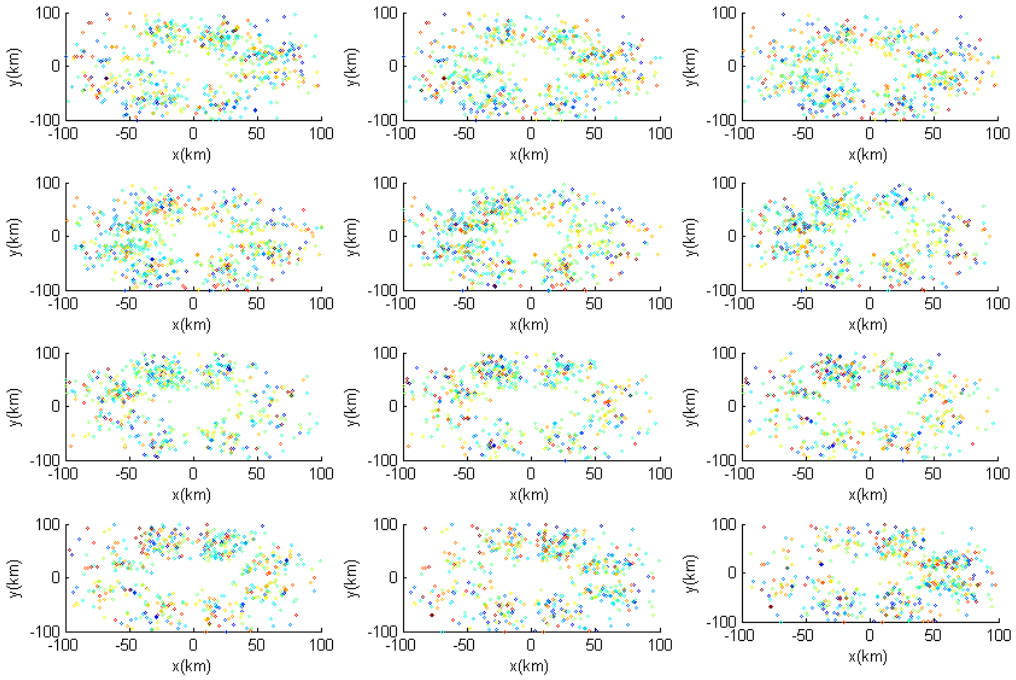

Figure 4.6:
Meteor plot perturbed line of sight velocity from September 10th, 2012. Top left plot is meteors from 01:00 to 02:00 fitted from 00:00 to 03:00, middle plot from 02:00 to 03:00 all the way to bottom right: 12:00 to 13:00. All times in CET

Figure(4.6) is an example of a meteor plot where the background wind has been removed. The colors on each dot now represent the perturbed line of sight velocity primarily due to gravity waves. The color bar was set to $\pm 30 \frac{m}{s}$ to better display areas with larger variance in the perturbed line of velocities which means wave activity.

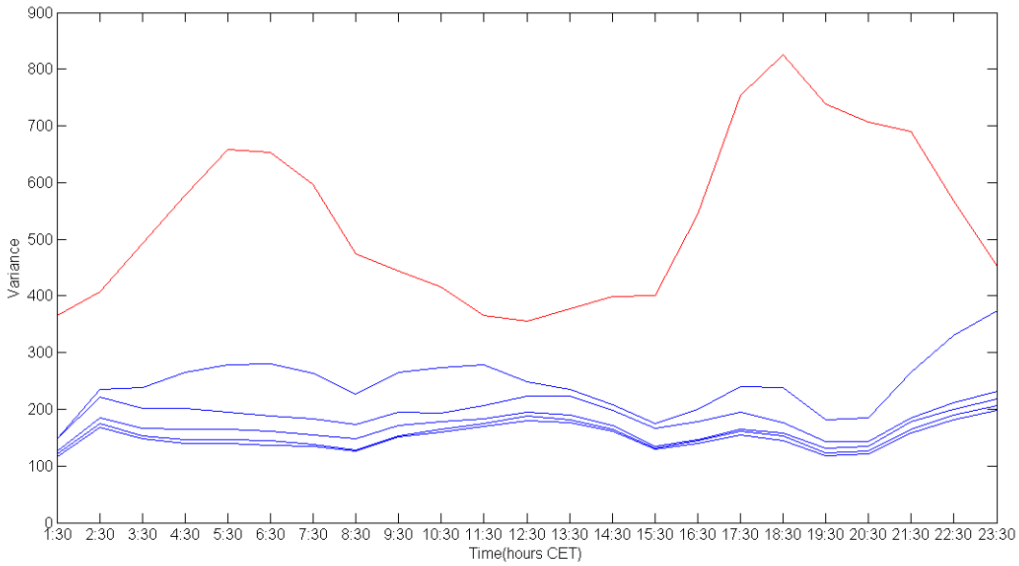

Figure 4.7:
Variance plot for the 10th of September with different vertical resolutions for the fitting routine.

Figure(4.7) is an hourly mean variance plot, where the variance in line of sight velocity has been measured over the entire field of view. The red line with the largest values corresponds to the variance in the line of sight velocity before the background wind has been removed. The blue line just below shows the variance of the perturbed line of sight velocity where the fit was made to the entire set of data at once, so its vertical resolution was 8 kilometres. The one below had its fit made to two height intervals each of 4 kilometres. The three remaining blue lines has from top to bottom vertical resolutions of 2 kilometres, 1 and 0,5 kilometre. It is clear from figure(4.7) that the three smallest vertical resolutions are all very close to the best possible fit. Which again is why a vertical resolution of 2 kilometres was chosen.

4.3 Total variance and net directional variance

After the data has been filtered and background wind removed, measures of gravity wave behaviour can be made. In this thesis 2 measures of gravity wave behaviour will be done, one gives wave "activity", the other wave direction. The 2 methods are respectively the total variance method and the net directional variance method.

4.3.1 Total variance

The total variance method consist of measuring the variance in the perturbed line of sight velocity over the entire field of view hour by hour. This gives the hourly wave "activity" which is shown for September the 10th in figure(4.8).

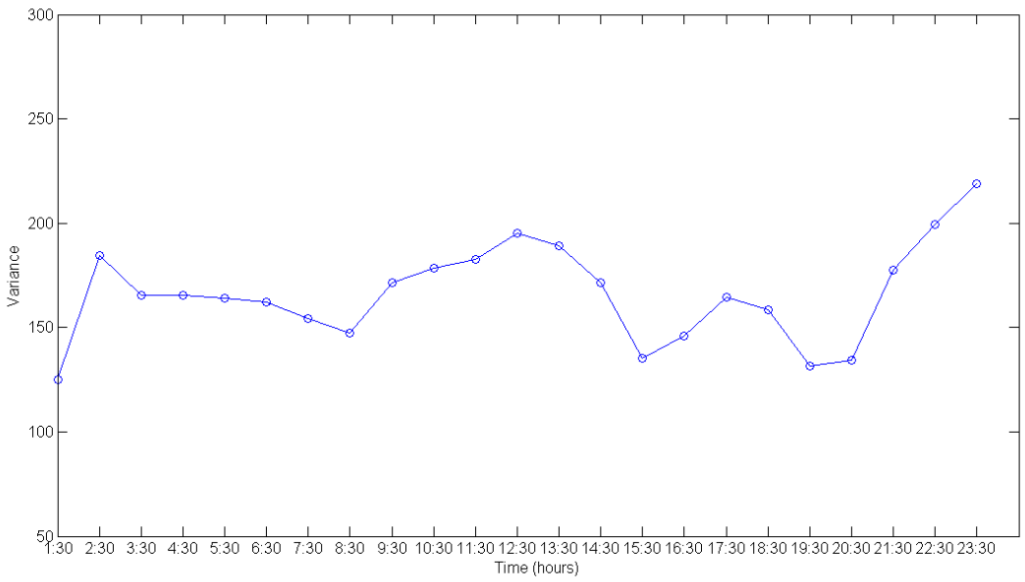

Figure 4.8: *Total variance plot on hourly time scale from the 10th of September. Time is in CET (Central European standard time)*

The time period at which the total variance will be looked at in this thesis is daily. This means that the hourly variance needs to be averaged

24 hours at a time. Variances form a "log-normal" distribution, so they can't be averaged as they are measured. To average variances, the logarithm needs to be taken on the entire data set. This makes the distribution into a "normal" distribution. After averaging, the data is converted back by taking the exponential, see e.g. Mithcell and Beldon [2]. The resulting average daily variance plot is shown in figure(5.1).

4.3.2 Net directional variance

The net directional variance is found by evaluating the variance in one half of the sky (for example the upper half in figure(4.2)), then subtracting it from the variance of the other (bottom) half. This can be done in eight directions and plotted hour by hour. Net directional variance plots display both wave direction as well as wave strength. Figure(4.9) shows a net variance plot from September the 10th.

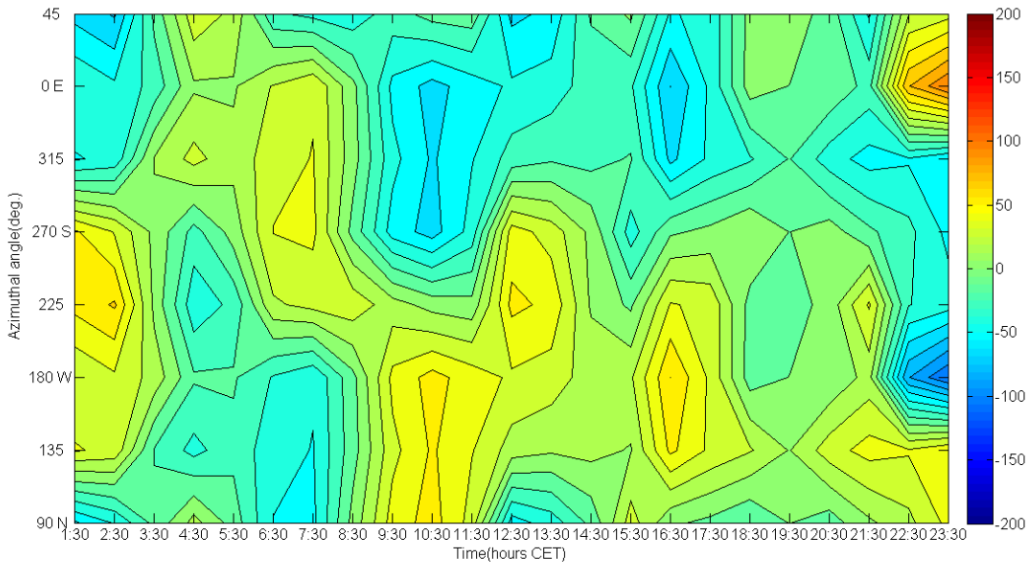

Figure 4.9:
Net variance in line of sight velocity plotted as a function of azimuthal angle and time for 10th of September.

The yellow and red spots in figure(4.9) represents positive net variance. These areas show propagation direction and strength of wave activity at a

certain time. Figure(4.9) shows little wave activity until 22:00 when there is a sudden burst in wave activity towards the east for 1 and a half hour.

This thesis is a climatology with 234 days worth of meteor data. The net variance plots work well for 24 hours at a time, but for more than five days they become messy. The solution was to run through each hour extracting the direction corresponding to the largest "net variance" value. The resulting plots shows the most preferred wave direction as a dot for each hour.

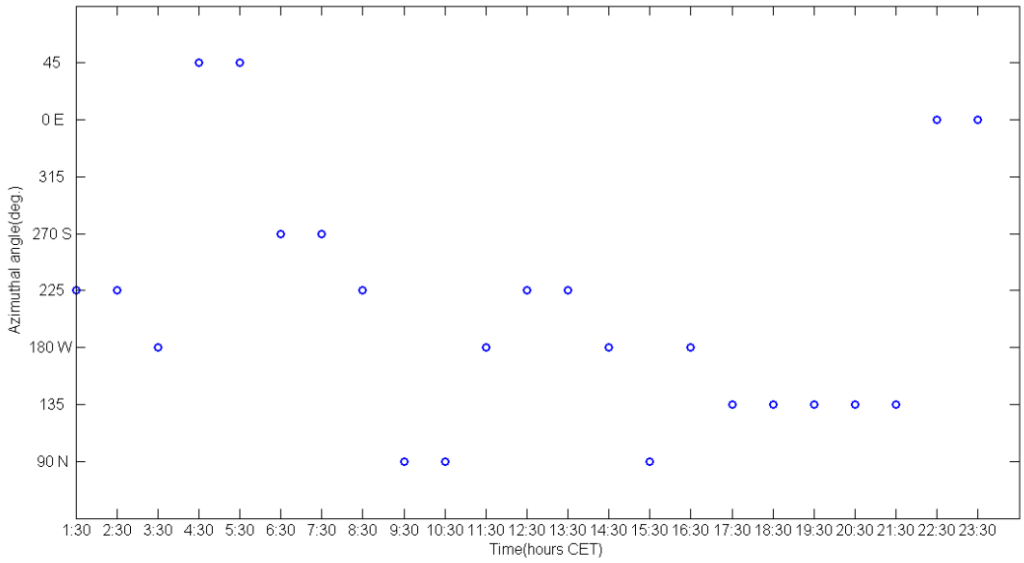

Figure 4.10:
Direction plot from September 10th.

It can be seen by comparing figure(4.9) and figure(4.10) that the preferred wave activity matches. The direction plots are not restricted to an hourly time scale, but can be measured for any give time period. This is done by looking at directions for the wanted time series of T hours and using the modal wave direction as the preferred wave direction.

In this thesis the direction plots will be looked at in time series of hourly, daily and weekly.

Chapter 5

Results and discussion

5.1 Total variance

The result obtained from the total variance method is a log-normal averaged daily variance plot for 234 days. It shows how the wave "activity" in the airglow layer over Trondheim has varied from start of fall until mid spring.

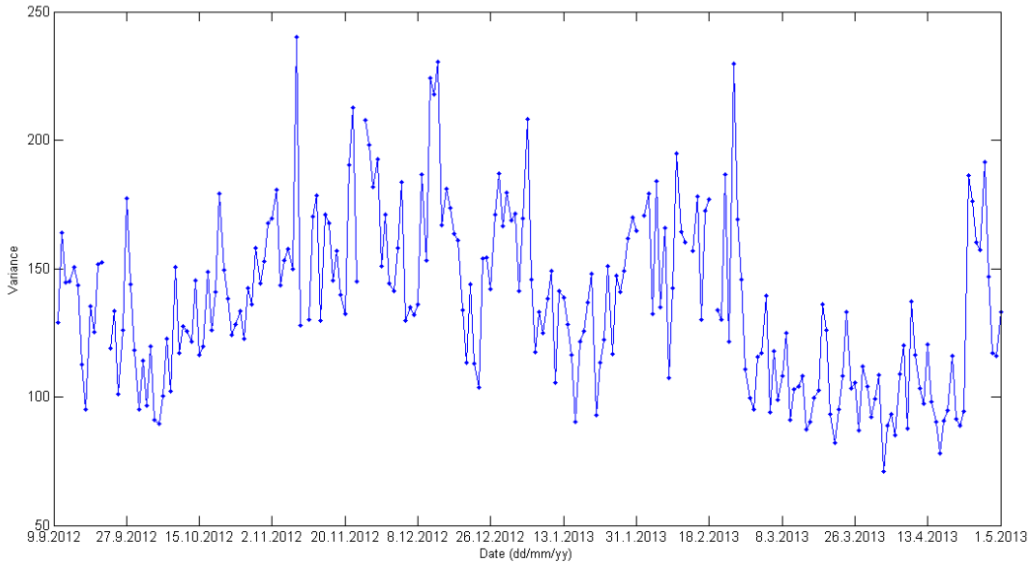

Figure 5.1:
The log-normal averaged daily variance plot from 9th of September until the 30th of April

The resulting figure(5.1) show two minima in variance around the equinoxes and a maxima between them mid winters. Figure(5.2) shows the monthly mean variance in perturbed line of sight velocity measured by meteor radars at Rothera (68^oS) in the Antarctica and Esrange (68^oN) in the Artic [3]. The time axis is six months shiftet on the plot from Rothera to make the plots comparable. By inspecting the monthly average variance between 86 and 88 km in both of the plots in figure(5.2) it is clear that the seasonal change in wave "activity" is the same as in figure(5.1). Since the latitudes of the meteor radars in Rothera and Esrange are similar to Trondheim's, the comparison confirms that the total variance method gives correct results.

Another thing to notice in figure (5.1) is the dip in variance start to mid January. This could possibly be related to the sudden stratospheric warming on 6th of January 2013, but is beyond this thesis to be discussed.

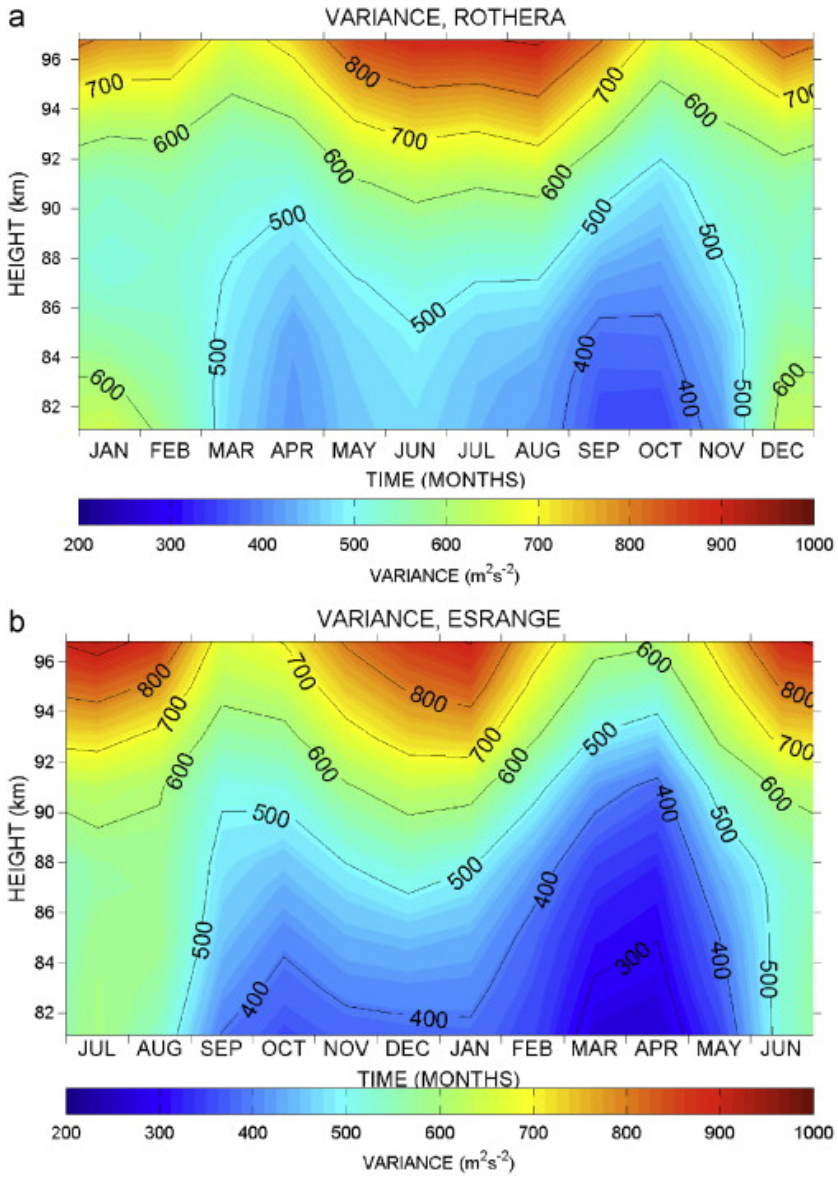

Figure 5.2:
Climatologies of monthly wave activity over a) Rothera and b) Esrange [3]

5.2 Net directional variance; Case studies and results

5.2.1 Comparison with airglow imager

Before the direction plots for the 234 day period are presented, they will be compared to other methods to make sure they work. The first case study is from the 3rd of December 2012, when large gravity waves were observed by the airglow imager at Dragvoll, Trondheim.

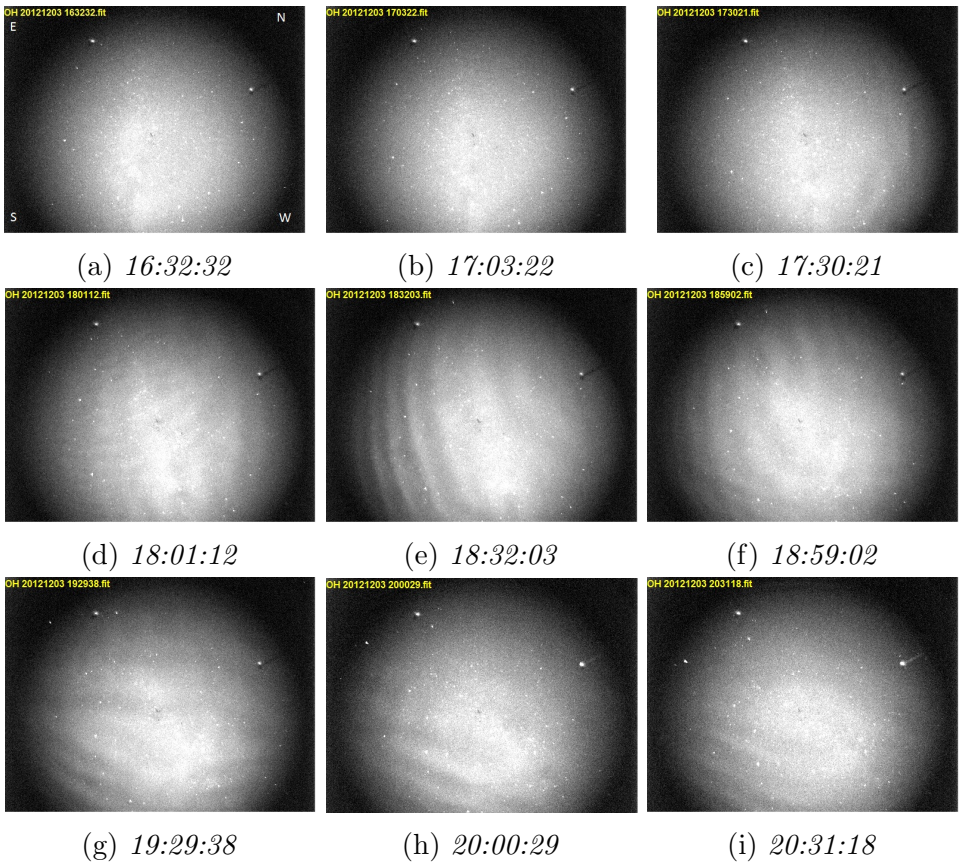

(a) *16:32:32* (b) *17:03:22* (c) *17:30:21*

(d) *18:01:12* (e) *18:32:03* (f) *18:59:02*

(g) *19:29:38* (h) *20:00:29* (i) *20:31:18*

Figure 5.3: *Time series of airglow images from December 3rd 2012. Directions are shown in the top left image. Time is in CET.*

Figure(5.3) shows the wave activity recorded by the airglow imager at Dragvoll on December the 3rd. From the figure it is possible to conclude that

the wave activity starts at 17:30 (5.3c). The waves propagate east to south east from 18:00 until atleast 19:00. This is shown in pictures (5.3d),(5.3e) and (5.3f). The wave direction then changes direction to south west for one hour, pictures (5.3g),(5.3h) and (5.3i).

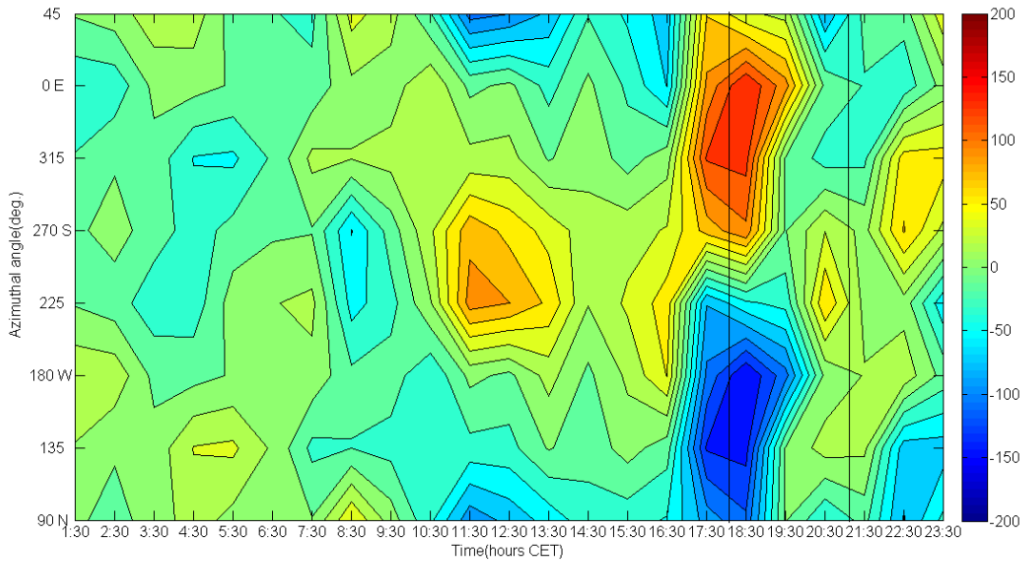

Figure 5.4:
Net direction variance plot from December the 3rd. The two vertical black lines represent the time period of 18:00 until 20:30.

The net directional variance plot shown in figure(5.4) shows little to no wave activity during the morning. There is a little burst to the south around 11:00, before a huge burst can be seen at 17:30 in the south east direction. The burst lasts for about 2 hours and is mostly south east and east. When the initial burst fades a wave activity rotation towards south west can be seen between 19:00 and 21:00. This is in good agreement with what was seen by the airglow imager in figure(5.3).

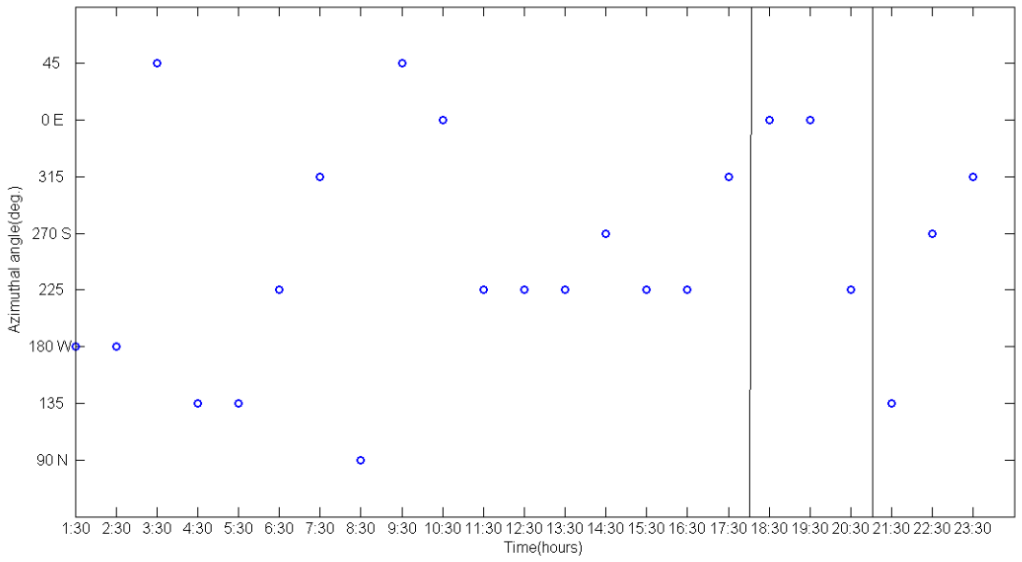

Figure 5.5:
Direction plot from December the 3rd. The two vertical black lines represent the time period of 18:00 until 20:30.

Figure(5.5) is the resulting direction plot from December 3rd. By inspecting the time of interest between the two vertical black lines it is possible to see that the directions agree with what is seen in figure(5.3) by the airglow imager. This is expected, since the direction plots are made from the data used in the net directional variance plots, which also agreed with the airglow imager.

We can conclude from this analysis that the meteor radar sees a burst of wave activity at the same time as the airglow imager with a propagation direction similar to the wave activity seen in the airglow imager.

5.2.2 Comparison with meteor plots

The other case study method is to look at areas in hourly direction plots where there is a constant preferred propagation direction. They represent a longer period of time where the wave activity is strongest one certain direction. By comparing the direction of a horizontal line in a direction plot with a meteor plot, it should be possible to see a larger variance in the given

direction at the given time in the meteor plot. Variance in meteor plots can be seen as higher density of red and blue dots in a certain direction.

By inspecting the last sub plot in figure(5.9), there is a straight horizontal line on the 17th of December. Direction plot of this day is shown in figure(5.6).

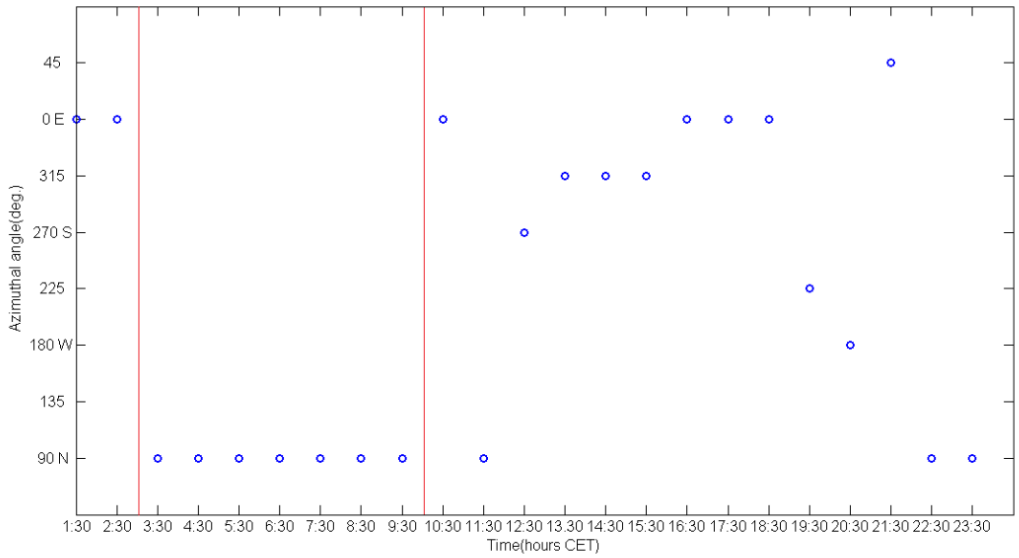

Figure 5.6: *Direction plot from 17th of December.*

The area of interest is as marked by the red vertical lines from 3 am until 9 am where the preferred wave direction is strictly north for the entire period.

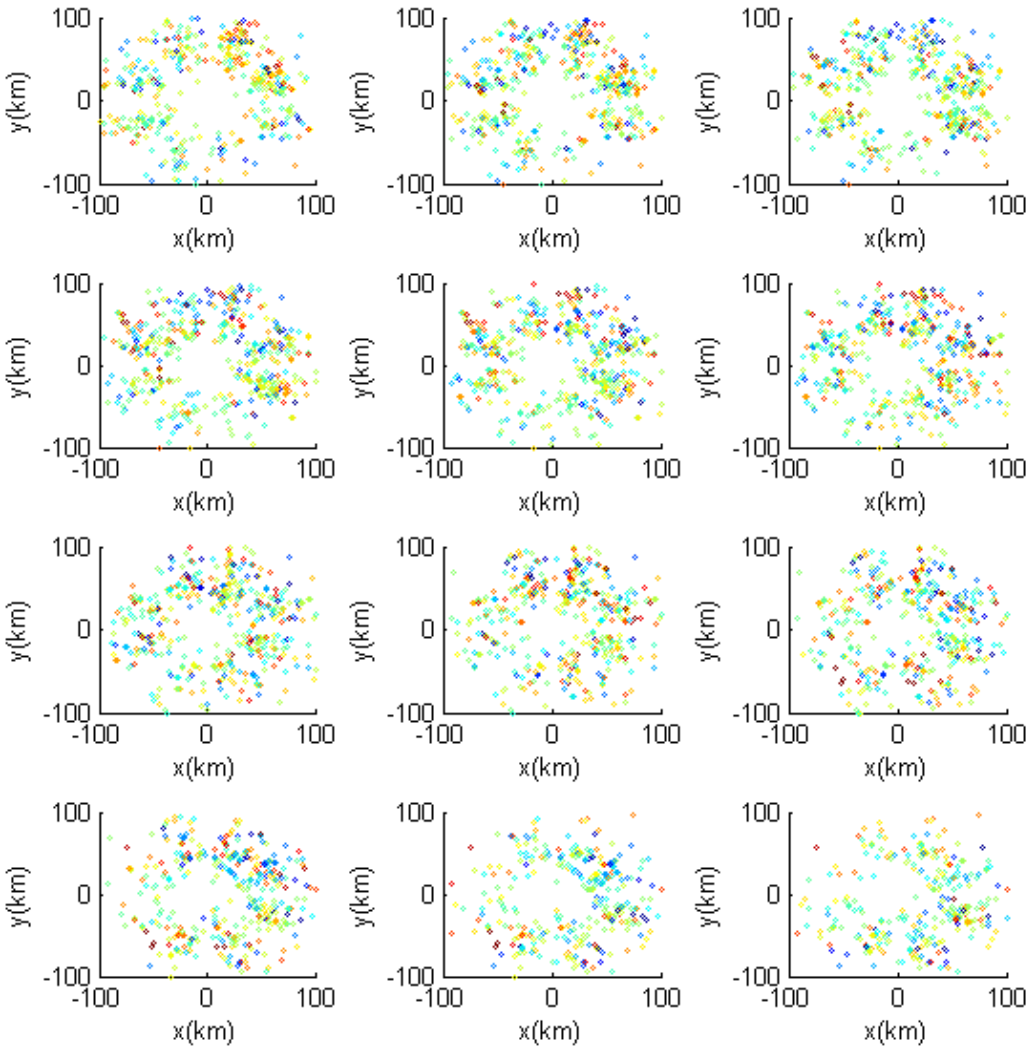

Figure 5.7: *Meteor plot of the 12 first hours from the 17th of December. Top left is from 01:00 to 02:00, top mid from 02:00 to 03:00 and so on until bottom right which is centred at 12:00 to 13:00.*

Looking at the meteor plot in figure(5.7), the northern(upper) half of the plots have a larger variance in the line of sight velocity than the southern(lower) half from 03:00 to 09:00. In the plots for the 2 first hours, 01:00 to 03:00, it is also possible to spot that the variance is largest towards the east, which also agrees with the direction plot.

From this analysis it is possible to conclude that the directions observed in the direction plots agree with the variance, primarily caused by wave activity, seen in the meteor plots.

5.2.3 Hourly time series

The following results are the hourly time series of the preferred wave direction for the entire data set from the 9th of September 2012 to the 30th of April 2013. The data is presented as the previous direction plots but also stacked on top of itself three times. This was done to better see continuous preferred wave direction rotations as the one showed by "(c)" in figure(5.9).

The hourly direction plots show the continuous wave directions changes caused by diurnal and semi-diurnal changes in the atmosphere, hence the tides. Several cases marked in red boxes are shown in the following figures displaying tides, noise and constant preferred wave direction.

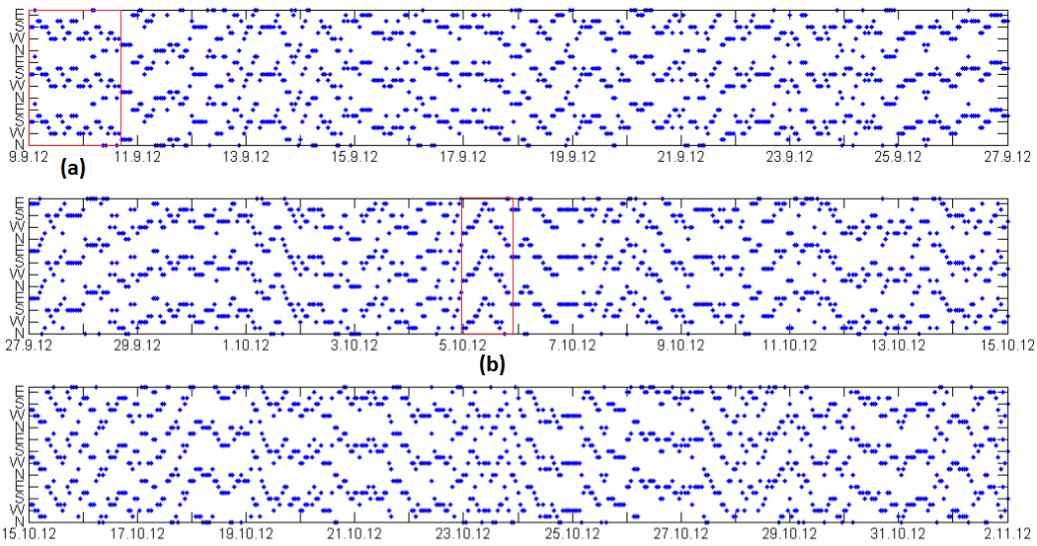

Figure 5.8: *Hourly direction plot from September 9th until 2th of November*

"(a)" represents a time period of almost 2 days where there is a relatively stable wave direction. "(b)" on the other hand shows a semi-diurnal counter clockwise rotation for the first 12 hours of February 5th, before it becomes a semi-diurnal clockwise rotation rest of the day.

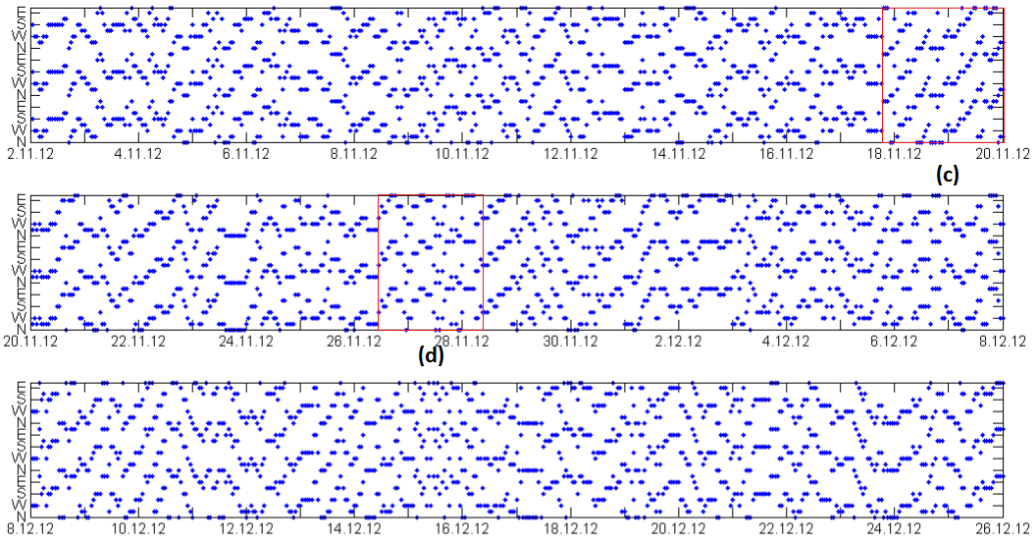

Figure 5.9: *Hourly direction plot from 2th of November until 26th of December*

The red box with the "(c)" label shows 2 day constant semi-diurnal counter clockwise rotation, and "(d)" shows a time period where there is no particular preferred pattern for one hour to the next (noise). Areas with no preferred propagation direction patters can mean 2 things, either there are no waves, or there are a lot of waves propagating in different direction.

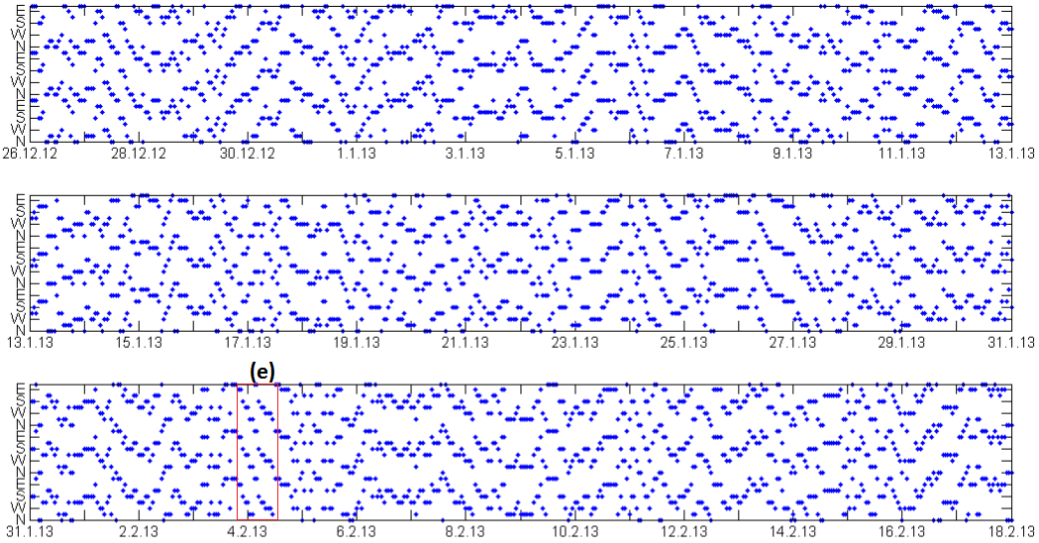

Figure 5.10: *Hourly direction plot from 26th of December until 18th of February*

"(e)" shows a very rapidly clockwise rotating wave direction, faster than semi-diurnal. Could possibly be caused by the ter-dirunal tide.

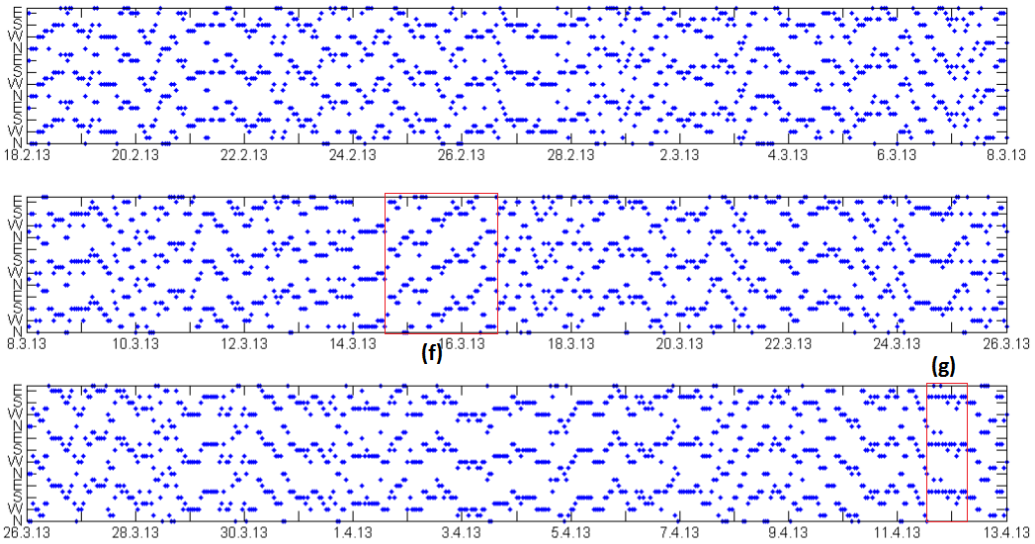

Figure 5.11: *Hourly Direction plot from 18th of February until 13th of April.*

A counter clockwise diurnal rotation can be seen in "(f)", while a strictly south eastwards preferred wave propagation direction for 10 to 15 hours is shown in "(g)".

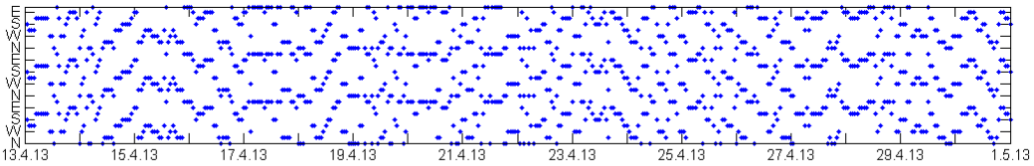

Figure 5.12: *Hourly Direction plot from 13th of April until 1st of May.*

5.2.4 Daily and weekly time series

Daily- and weekly direction plots were also made. The method consisted of taking the modal direction in one day or one week and use as the corresponding direction. The results are plots showing the most preferred wave direction for each day or each week.

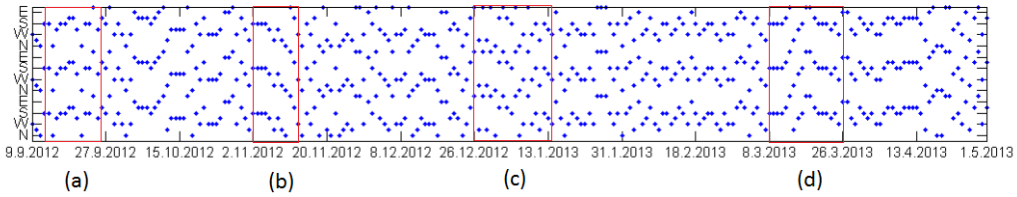

Figure 5.13: *Daily direction plot from 9th of September to 1st of May*

As with the hourly direction plots, figure(5.13) display some continuous directional changes in the preferred wave activity. The time period at which these changes occur are much longer than the changes in the hourly direction plots. Directional rotations shown in figure(5.13) will therefore correspond to periodic changes in the scale of several days. Phenomena in the atmosphere causing this behaviour could be planetary waves.

In figure(5.13) "(a)" marks a time period of several days where the preferred wave direction is relatively stable due south. "(b)" shows a week long clockwise rotation while "(c)" looks mostly like noise. "(d)" starts with 4

days strictly south west into a rapid week long counter clockwise rotation into a slow clockwise rotation.

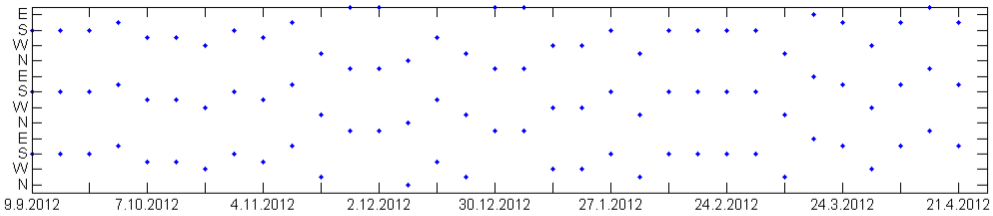

Figure 5.14: *Weekly direction plot from 9th of September to 1st of May*

Figure(5.14) displays a seasonal behaviour of the wave directions and all traces of tides and short period planetary waves are gone. The preferred gravity wave propagation direction is strictly south during autumn before getting more northwards during winter and then back to south again at the end of the winter. From the start of March until end of March it seems rotate clockwise 360^o from south to south again, while at the start of April it seems to start rotating anticlockwise.

5.3 Average monthly wave vectors

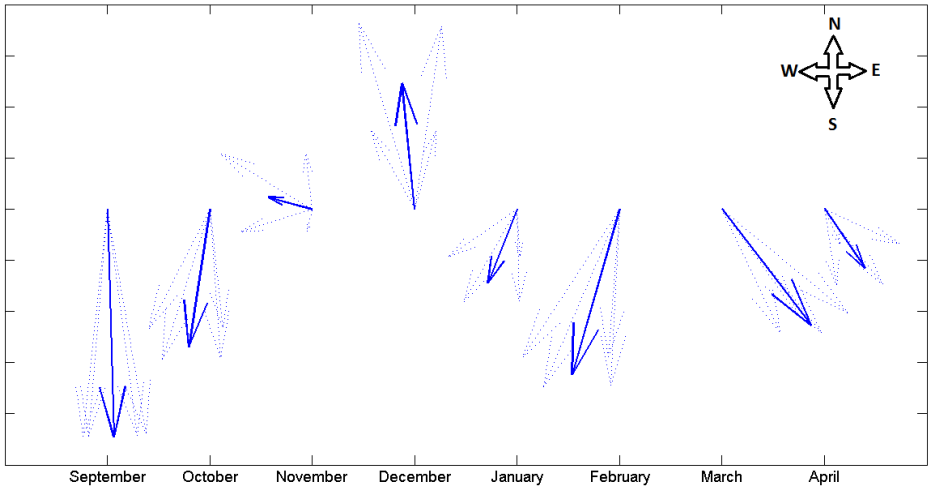

Figure 5.15:
Average monthly wave vector plot.

As a final result in this thesis is the average monthly wave vector plot shown in figure(5.15). Combining the direction plots with the variance plots, it shows the net wave activity and direction for each month from September 2012 until April 2013. The dashed blue arrows represent the standard error in the x and y direction.

The plot shows a southward preferred wave direction during the fall, rotating clockwise towards north in the start of winter. End of winter to start of spring shows a south-westwards propagation direction rotating anti-clockwise to south-east.

As the analysis has been restricted to altitudes corresponding to the airglow layer, the results presented here (5.15) should be directly comparable with airglow imager climatologies of gravity wave strength and direction. The next step is therefore to compare the results seen in figure(5.15) with results obtained by airglow imagers.

For example at Xinglong (40,2^{o}N, 117,4^{o}E) in northern China, where Li, Q et al. (2011)[19] observed a south westwards wave direction preference during the winter 2009/2010. This agrees with my result, where the three

vectors for December, January and February all have a westwards component, also summing the meridional components of the vectors would result in a southwards going vector giving my winter a south westwards preferred wave propagation direction.

A quick not before the next comparison: Many of the papers have results from the southern hemisphere. To be able to compare these results with mine, the months are shifted by 6 (e.g. November in the northern hemisphere is comparable with June in the southern), and the meridional components are in agreement when they are opposite, e.g. North is polewards in the northern hemisphere and south is polewards in the southern hemisphere.

Nielsen, K. et al. (2009)[20] at Halley, Antarctica (76^oS, 27^oW) observed wave propagation directions to be mostly westwards during fall, poleward during winter and eastwards during spring. These results partly agrees with mine. The zonal directions match, as my results also show a tendency towards west during the fall, and eastwards during the spring. The poleward preferred wave direction during winter however is completely opposite of my result.

Espy, P.J. et al. (2006)[22][23] observed at both Rothera(67^oS, 68^oW) and Halley (76^oS, 27^oW) a seasonal preferred wave direction rotating from north west to south west during winter. The zonal direction agrees with my result in this case, but the meridional directions are completely opposite.

Mereidos, A.F. et al. (2003)[24] observered from Cachoeira Paulista, Brazil(23^oS, 45^oW) a north westwards propagation direction during winter as well as abrupt changes in the directions around the equinoxes. In this case the meridional propagation direction agrees with my result. Any abrupt change in wave direction around equinoxes can however not be seen in figure(5.15). This could be due to the vectors being averaged over an entire month. Inspecting figure(5.14), which has a smaller time resolution, it is possible to see some abrupt changes in directions mid November and start of March. This is in agreement for the spring equinox, but the abrupt change during fall comes after the equinox in my results.

Some papers only presented results for the summer months. These are not comparable with my results, but will be presented briefly anyway.

Paulet, PD et al. (2005)[21] observed from two different locations in northern Australia; Wyndham ($15{,}5^oS$, $128{,}1^oE$) and Katherine ($14{,}5^oS$, $132{,}3^oE$), during a ten day period in November, (the first summer month,) 2001 that $\frac{3}{4}$ of the wave activity was propagating southwards (polewards).

Taylor, M.J. et al. (1993)[27] observed northwards (polewards) and eastwards wave directions during the summer months. The observations were

made from Mountain Research Station (40^oN, 106^o W, 3050 m), near Nederland, Colorado.

Gravity wave climatologies have also previously been done using meteor radars. The data analysis differs from mine, but the results are comparable.

Fritts, D.C. et al. (2010)[25] has made a climatology using The Southern Argentina Agile Meteor Radar (SAAMER), located on Tierra del Fuego (53.8^oS). The results agrees with mine for fall and spring with north east during September and north west during March. During winter Fritts, D.C et al. sees the propagation direction to be north east wards. The meridional component agrees with my results but the zonal is completely opposite.

Hocking, W.K. (2005)[26] measures the average zonal wave direction for the period April 2002 until January 2005. The radar used to generate the results is a SKiYMET meteor radar located at Socorro, New Mexico, in the USA (34^oN, 107^oW). At 87km, Hocking's results show a clear tendency to eastwards propagation direction during winter and west wards during summer. His results show the opposite directions compared to mine.

Chapter 6

Summary and future work

In this thesis a meteor radar located at Dragvoll (64,4^{o}N, 10,5^{o}E) in Trondheim has been used to make a gravity wave climatology for the autumn to spring season 2012/13. The gravity wave climatology consisted of both a wave direction study as well as a wave activity study. Wave directions were determined by measuring the variance in the perturbed line of sight velocity in one half of the sky and then subtracting if from the variance in the other half. The wave activity results were made looking at the variance in the perturbed line of sight velocity over the entire field of view. Both wave activity and directions were looked at in different time series, from hourly, daily and weekly. As a final result in this thesis a monthly average wave vector plot was made, combining both studies.

Comparing the results achieved in this thesis with results in similar studies using an airglow imager shows both agreement and disagreement. Both methods have advantages and disadvantages over the other. The airglow imager observed the wave direction directly, which can not be done with the meteor radar. An airglow imager is however only operational during night time with a clear sky. The meteor radar can run 24 hours 365 days a year. A meteor radar can also be used to quantify wave activity which is more difficult with an airglow imager.

Future work could consist of doing a more thorough study of the hourly direction plots. Look at the different continuous changes and try and find the corresponding tide, wave or maybe something else. Another interesting study would be to look at the noisy areas in the direction plots and see if there is any correlation between them and the wave activity. As a final thing, it would be interesting to take a closer look at the variance dip in figure(5.1)

around start of January and see if it is a stratwarming causing it.

Bibliography

[1] Hocking, W.K., et al. "Real time determination of meteor-related parameters utilizing modern technology" *Journal of Atmospheric and Solar-Terrestrial Physics*, 63 (2001) 155-169.

[2] Michell, N.J., Beldon, C.L., "Gravity waves in the mesopause region observed by meteor radar: 1. A simple measurement technique", *Journal of Atmospheric and Solar-Terrestrial Physics* 71 (2009) 866-874.

[3] Mitchell, N.j., Beldon, C.L., "Gravity waves in the mesopause region observed by meteor radar, 2: Climatologies of gravity waves in the Antarctic and Arctic." *Journal of Atmospheric and Solar-Terrestrial Physics* 71 (2009) 875-884.

[4] Nielsen, K., et al. "Climatology of short-period mesospheric gravity waves over Halley, Antarctica (76°S, 27°W)", *Journal of Atmospheric and Solar-Terrestrial Physics* 71 (2009) 991-1000

[5] Hocking, W.K., et al. "Comparison of meteor radar and Na Doppler lidar measurements of winds in the mesopause region above Maui, Hawaii", *Journal of geophysical reasearch* Vol. 110, D09502, doi: 10.1029/2003JD004486, 2005.

[6] Yoshimoto, Hitoshi , "Wave Dynamics on the Mesospheric Hydroxyl Layer" CL-TR-90-0211, 01.02.1990.

[7] Vincent, Robert A. "Gravity wave coupling from below: A review". *Climates and Weather of the Sun-Earth coupling-system (CAWES)* Selected papers from 2007 Kyoto Symposium, pp. 279-293.

[8] Hocking, W.K., www.physics.uwo.ca/ whocking/p103/grav-wav-html/.

[9] SKiYMET Meteor Radar Reference Manual Version 2.0

[10] home.phys.no/brukdef/prosjekter/atmosfys/web-pages/SKiYMET-flux.php

[11] home.phys.no/brukdef/prosjekter/atmosfys/web-pages/SKiYMET-wind.php

[12] Singer, W., et al. "Diurnal and annual variations of meteor rates at the arctic circle". *Atmospheric Chemistry and Physics*, Vol. 4. 1355-1363, 2004.

[13] Vincent, R.A., Reid, I.M., "HF Doppler Measurements of Mesospheric Gravity Wave Momentum Fluxes".*Journal of the Atmospheric Science* Vol. 40, 1321-1333, 1983.

[14] Fritts, D.C., et al. "(2010), Southern Argentina Agile meteor radar: System design and initial measurements of large scale winds and tides". *Journal of Geophysical Research.*, 115, D18112, doi:10.1029/2010JD13850.

[15] D. C. Fritts et al. "Southern Argentina Agile Meteor Radar: Initial assessment of gravity wave momentum fluxes" *JOURNAL OF GEOPHYSICAL RESEARCH, VOL. 115, 2010*

[16] www.srh.noaa.gov/jetstream/atmos/atmprofile.htm

[17] N.J. Mitchell et al. "Mean Winds and tides in the Arctic mesosphere and lower thermosphere." (2002)

[18] Jeffery M. Forbes "Vertical coupling by the semidiurnal tide in Earth's atmosphere."

[19] Li, Q. et al. "Statistical characteristics of gravity wave activity observed by an OH airglow imager at Xinlong, in norhtern China." (2011).*ANNALES GEOPHYSICAE Volume: 29 Issue: 8 Pages: 1401-1410*

[20] Nielsen, K. et al. "Climatology of short-period mesospheric gravity waves over Halley, Antarctica." (2009) *Journal of Atmospheric and Solar-Terrestrial Physics 71 Issue 8-9 Pages 991-1000.*

[21] Paulet ,P.D. et al. " Climatology of short-period gravity waves observed over northern Australia during the Darwin Area Wave Experiment (DAWEX) and their dominant source regions" (2005) *JOURNAL OF GEOPHYSICAL RESEARCH-ATMOSPHERES Volume: 110 Issue: D3 Article Number: D03S90*

[22] Espy, P.J., et al. "Regional variations of mesospheric gravity-wave momentum flux over Antarctica." *ANNALES GEOPHYSICAE Volume: 24 Issue: 1 Pages: 81-88 Published: 2006*

[23] Espy, P.J., et al. "Seasonal variations of the gravity wave momentum flux in the Antarctic mesosphere and lover thermosphere.".*JOURNAL OF GEOPHYSICAL RESEARCH-ATMOSPHERES Volume: 109 Issue: D23 Article Number: D23109 DOI: 10.1029/2003JD004446 Published: DEC 8 2004*

[24] A. F. Medeiros et al. "An investigation of gravity wave activity in the low-latitude upper mesosphere: Propagation direction and wind filtering" *JOURNAL OF GEOPHYSICAL RESEARCH, VOL. 108, 2003*

[25] D. C. Fritts et al. "Southern Argentina Agile Meteor Radar: Initial assessment of gravity wave momentum fluxes" *JOURNAL OF GEOPHYSICAL RESEARCH, VOL. 115,D19123, doi:10.1029/2010JD013891, 2010*

[26] W. K. Hocking. "A new approach to momentum flux determinations using SKiYMET meteor radars" *Annales Geophysicae, 23, 24332439, 2005 SRef-ID: 1432-0576/ag/2005-23-2433 European Geosciences Union 2005*

[27] EVIDENCE OF PREFERENTIAL DIRECTIONS FOR GRAVITY-WAVE PROPAGATION DUE TO WIND FILTERING IN THE MIDDLE ATMOSPHERE Author(s): TAYLOR, MJ (TAYLOR, MJ); RYAN, EH (RYAN, EH); TUAN, TF (TUAN, TF); EDWARDS, R (EDWARDS, R) Source: *JOURNAL OF GEOPHYSICAL RESEARCH-SPACE PHYSICS Volume: 98 Issue: A4 Pages: 6047-6057 DOI: 10.1029/92JA02604 Published: APR 1 1993*

[28] Lund, H. "Variations in the hydroxyl layer near infrared airglow at Rothera, Antarctica (68^{o}S, 68^{o}W)" *Master's thesis at NTNU, Faculty of Natural Science and Technology, Department of Physics 2010.*

Appendix A

Results presented at EGU 2013

Some of the results in this thesis were presented at the European Geosciences Union General Assembly 2013 in Vienna; http://www.egu2013.eu/home.html.

Figure(A.1) on the next page shows a pdf that was presented at the EGU 2013. The right part of the sheet (after turning this thesis 90^o counter clockwise) shows both the case study of 3rd of December, comparing meteor radar results with an airglow imager, as well as direction plots and total variance plots.

Comparison of gravity wave momentum flux observed by meteor radar and airglow imager

Robert Hibbins, Rosmarie de Wit, Patrick Espy, Nils Kolnes, Magnus Svennevik (NTNU),
Gary Swenson, Fabio Vargas (Univ Illinois)

NTNU – Trondheim
Norwegian University of Science and Technology

Contact: robert.hibbins@ntnu.no

Abstract

A new 30 kW SkiYMET meteor radar has been operational at Trondheim, Norway (63°N, 10°E) during the winter of 2012-13. The transmitter array is designed to direct the majority of the radar power into eight beams at 45° azimuth increments with peak power around 35° off-zenith. Meteor count rates up to 15000 per day are observed with this system. Co-located with the radar is an all-sky camera filtered to observe perturbations in the hydroxyl airglow layer due to gravity waves. High temporal resolution observations reveal the horizontal wavelength, amplitude and propagation speed and direction of gravity waves as they pass through the airglow layer. During clear-sky conditions clearly-defined gravity wave structure is frequently observed in the hydroxyl airglow. We compare the strength and direction of gravity wave activity imaged in the airglow with estimates of the vertical flux of horizontal momentum derived from the line of sight meteor drift perturbation velocities observed in the radar.

Trondheim meteor radar example data

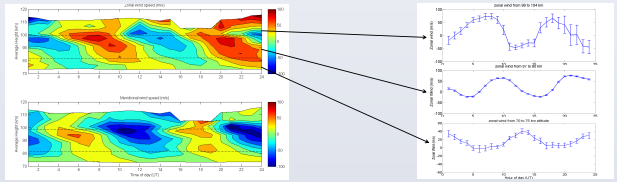

Hourly mean winds can be derived from the radar between ~74 and 105 km. Here an example day's data is shown as a contour plot (left panel) and as hourly mean zonal wind derived from the meteor trail drift velocities recorded between 70-75 km, 87-90 km and 99-104 km (right panel). 2σ error bars are shown. Clearly defined semidiurnal tides can be seen across the range of altitudes.
See http://home.phys.ntnu.no/brukdef/prosjekter/atmosfys/web-pages/SKiYMET-flux.php for more data

Comparison with airglow imager data

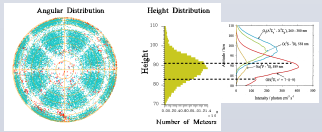

We restrict our analysis to meteor trail velocities recorded between altitudes of 83 and 91 km to coincide with the OH airglow layer centred around 87 ± 4 km altitude. Within this limited altitude range we typically observe around 4000 individual unambiguous meteor echoes per day at zenith angles less than 60°.

Fitted hourly mean horizontal wind is subtracted off the unambiguous line-of-sight meteor drift velocities recorded during that hour, then the variance in the residual line of sight velocities of the meteors recorded in one azimuthal direction is subtracted from that recorded in the opposite direction as a measure of the gravity wave momentum flux within the airglow layer (e.g. Vincent & Reid JAS, 40, 1321-1333, 1983). The momentum flux thus derived can be compared with wave activity observed in the airglow imager during cloud-free conditions.

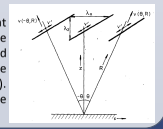

Case study: December 3rd 2012

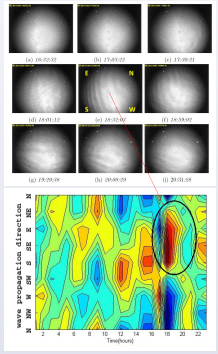

The airglow imager is co-located with the meteor radar. All-sky OH 6-2 vibrational band data are recorded through a broad-band NIR filter centred on 840 (±20) nm for a 90 s integration repeated every four minutes when the sun is >10° below the horizon.

During the evening of December 3rd 2012 the airglow imager recorded a clear quasi-monochromatic gravity wave propagating towards the south east. The wave first appears in the airglow images at around 18:00 UT and persists until approximately 20:30 UT. Prior to 18:00 UT no strong horizontally-propagating wave activity was observed in the airglow images. The nine panels to the left show frames from the airglow imager spaced at approximately half-hour intervals between 16:30 and 20:30 UT.

The bottom panel shows the net variance in the residual line-of-sight meteor drift velocities as a function of azimuthal angle during the 22 hours between 01:00 UT and 23:00 UT on 3rd December 2012. Coincident with the onset of the SE propagating gravity wave seen in the airglow imager is a burst of momentum flux towards the SE direction lasting approximately 2 hours between 18:00 and 20:00 UT. The gravity wave perturbations clearly seen in the OH airglow layer are also seen to perturb the individual meteor trail line-of-sight velocities - most strongly in the direction of wave propagation.

Gravity wave activity during the 2012-13 winter

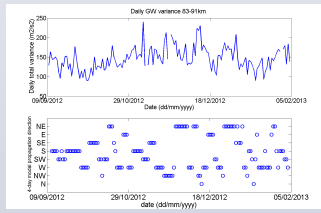

Preliminary analysis of the gravity wave activity observed in the line-of-sight meteor perturbation velocities throughout the 2012-13 autumn and winter within the OH airglow layer shows an increase in GW variance during the early winter following an autumn minimum (top panel). GW directions within this layer are typically southwards and eastwards during September and October turning polewards by mid-winter.

This mid-winter poleward wave activity is also reported in airglow imager data recorded during the winters of 2001-2 from Halley station, Antarctica (76°S, 27°W) - Nielsen et al., JASTP 71, 991–1000, 2009.

The effects of the 2013 sudden stratospheric warming on GW momentum flux in the MLT above Trondheim are discussed in an accompanying poster (de Wit et al., EGU2013-1589).

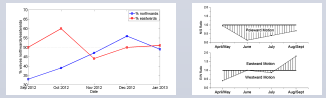

Figure A.1:
A copy of the presentation made for EGU 2013.

Appendix B

Matlab code

B.1 Reading the data

```
function LesDataWT = LesDataWTD(x)    %Reads a data file x, returns a matix
                                      %called LesDataWT.

%Define format of datafile, "%s" means string column and "%f" means
%number (double) column. The "*" means "don't read".
format='%s %s %*s %f %f %f %f %f %f %f %f %f %f %f %f %f %f';

% Open file
fid = fopen(x);
if fid == -1;
    disp ('Could not open file')
% Read file starting from line 30
else
    C = textscan(fid,format,'HeaderLines',29);
    C{1,2}=strrep(C{1,2},':','');    %removes ":" from the time string
    C{1,2}=str2double(C{1,2});       %converts time string to a double
    C{1,1}=strrep(C{1,1},'/','');    %removes "/" from the date string
    C{1,1}=str2double(C{1,1});       %converts date string to a double.
    LesDataWT=cell2mat(C);           %converts the cell to a matrix.
end

closeresult = fclose(fid);
if closeresult == 0
    disp ('File closed')
else
    disp ('File not closed')
end
end
```

B.2 Filtering the data

```
function FilterAmbigH = FilterAmbigHTheta(x,hmax,hmin)
```

```
%Filters out Ambigous results, meteors outside height intervall and meteors
%with a larger theta than 60 degrees.
a = (length(x(:,8)));
FilterAmbigH=[a,16];
for i = 1:a
    if x(i,9)== 1 && x(i,4)<=hmax && x(i,4)>=hmin && x(i,7)<=60
        for j = 1:16
            FilterAmbigH(i,j)=x(i,j);
        end
    end
end
end
```

B.3 Fitting the background wind

```
function [fitresult, gof] = createSurfaceFit(Xf, Yf, Vf)
%CREATESURFACEFIT(XF,YF,VF)
%  Fit surface to data.
%
%  Data for 'Test sf' fit:
%      X Input : Xf
%      Y Input : Yf
%      Z Output: Vf
%  Output:
%      fitresult : an sfit object representing the fit.
%      gof : structure with goodness-of fit info.
%
%  See also FIT, SFIT.

%  Auto-generated by MATLAB on 16-Oct-2012 11:43:59


%% Fit: 'Test sf'.
[xInput, yInput, zOutput] = prepareSurfaceData( Xf, Yf, Vf );

% Set up fittype and options.
ft = fittype( '+U.*sin(y)*cos(x)+V.*sin(y)*sin(x)',...
    'indep', {'x', 'y'}, 'depend', 'z' );
opts = fitoptions( ft );
opts.Display = 'Off';
opts.Lower = [-Inf -Inf];
opts.StartPoint = [0.616382333448512 0.27293957962843];
opts.Upper = [Inf Inf];

% Fit model to data.
[fitresult, gof] = fit( [xInput, yInput], zOutput, ft, opts );

%fitresult

% Make contour plot.
%%figure( 'Name', 'Test sf' );
%%h = plot( fitresult, [xInput, yInput], zOutput, 'Style', 'Contour' );
%%legend( h, 'Test sf', 'Vf vs. Xf, Yf', 'Location', 'NorthEast' );
% Label axes
```

```
%%xlabel( 'Xf' );
%%ylabel( 'Yf' );
%%grid on
```

B.4 Net directional variance and direction plots

```
Files=dir('Datafiler'); Folder='Datafiler\'; TotData=[];
hmin=83; hmax=91; hint=2;              %Define height interval size and
n=(hmax-hmin)/hint;                    %max and min height.
numberOfDays=234;
for i = 3:numberOfDays+2;              %Reads all the files.
    CombStr=strcat(Folder,Files(i).name);
    Data=LesDataWTD(CombStr);
    Data(:,2)=Data(:,2)+(i-3)*240000;
    FData=FilterAmbigHTheta(Data,hmax,hmin);
    FData(all(FData==0,2),:)=[];
    TotData=[TotData;FData];           %Saves each day in a single matrix.
end                                    %Initialising variables.
PHI00=(TotData(:,8)/360)*2*pi;THETA00=(TotData(:,7)/360)*2*pi;
LOS00=TotData(:,5);RANGE00=TotData(:,3);HEIGHT00=TotData(:,4);
T0=TotData(:,2);U=zeros(24*numberOfDays,n);V=zeros(24*numberOfDays,n);
VAR0=zeros(8,24*numberOfDays);VAR1=zeros(8,24*numberOfDays);
AVGVAR=zeros(8,numberOfDays);GOF=zeros(24*numberOfDays,n);
T=zeros(length(LOS00),1);X=zeros(length(LOS00),1);
Y=zeros(length(LOS00),1); DELTALOS=zeros(length(LOS00),1);
PHI0=zeros(length(PHI00),1);THETA0=zeros(length(PHI00),1);
LOS0=zeros(length(PHI00),1);RANGE0=zeros(length(PHI00),1);
flag=0;
N=zeros(8,1);L=0;n=1;
figure;
for l = 1:n                            %Sort height into hint km intervals
    HH=find(HEIGHT00<=(hmin+hint*l) & HEIGHT00 >=((hmin-hint)+hint*l));
    PHI0(HH)=PHI00(HH);
    THETA0(HH)=THETA00(HH);
    LOS0(HH)=LOS00(HH);
    RANGE0(HH)=RANGE00(HH);
    T(HH)=T0(HH);
    for k = 1:24*numberOfDays          %Step hour by hour, finding indecies.
        BB=find(T<=(2+k)*10000 & T>(k-1)*10000 & T~=0);
        CC=find(T<=(k+1)*10000 & T>(k)*10000);
        if length(BB)<=1;              %Keep tracks of discontinuous data.
            flag=flag+1;
            continue
        end                            %Store corresponding variables:
        PHI=PHI0(BB);
        THETA=THETA0(BB);
        LOS=LOS0(BB);
        RANGE=RANGE0(BB);
        PHI1=PHI0(CC);
        THETA1=THETA0(CC);
        LOS1=LOS0(CC);
        RANGE1=RANGE0(CC);             %Make the fit:
        [fitresult, gof] = createSurfaceFit(PHI,THETA,LOS);
        U(k,l)=fitresult.U;
        V(k,l)=fitresult.V;
```

```
        L=L+length(CC);
        if k == 696*n                    %This gets the number of meteors in
            N(n)=L;                      %each month and saves it in N.
            L=0;
            n=n+1;
        end
        for j = 1:length(CC);            %Removes the fitted backg. wind:
            DELTALOS(CC(j))=LOS1(j)-(U(k,l)*sin(THETA1(j))*cos(PHI1(j))...
            +V(k,l)*sin(THETA1(j))*sin(PHI1(j)));
            X(CC(j))=sin(THETA1(j))*cos(PHI1(j))*RANGE1(j);
            Y(CC(j))=sin(THETA1(j))*sin(PHI1(j))*RANGE1(j);
        end
    end
    T=zeros(length(PHI00),1);
end
for k =1:24*numberOfDays                 %Steps through hour by hour again
    BB=find(T0<=(2+k)*10000 & T0>=(k-1)*10000);
    DELTALOS3=DELTALOS(BB);              %Find corresponding pert.los velocity
    X3=X(BB);
    PHI1=PHI00(BB);
    LOS3=LOS00(BB);
    Y3=Y(BB);
    for i =1:4                           %Steps through half of the directions
        AA=find(PHI1<=(pi/4)*(3+i) & PHI1>=(i-1)*(pi/4));%Taking four and
        CC=zeros(length(PHI1),1);        %four slices each time.
        CC(AA)=PHI1(AA);                 %Get indecies from half of the sky.
        DD=PHI1-CC;
        EE=find(DD~=0);                  %Get indecies for other half of sky.
        DELTALOS00=DELTALOS3(AA);        %Get the corresponding pert.los velo's.
        DELTALOS000=DELTALOS3(EE);
        NETVAR=var(DELTALOS00)-var(DELTALOS000);
        VAR0(i,k)=NETVAR;                %Stores the calculated NETVAR's in a
        VAR0(i+4,k)=-NETVAR;             %matrix.
        LOS1=LOS3(AA);
        LOS2=LOS3(EE);
        NETVAR1=var(LOS1)-var(LOS2);%NETVAR without removing backgr.wind.
        VAR1(i,k)=NETVAR1;
        VAR1(i+4,k)=-NETVAR1;
        NETVAR=0;NETVAR1=0;              %reset variables.
    end
end
directionMatrix2=zeros(numberOfDays*24,1);
for i=1:numberOfDays*24                  %Make the array for the direction plots
    [x,y]=max(VAR0(:,i));
    directionMatrix2(i)=y;
end
                                         %Plotting routines for Net variance
                                         %plots and direction plots
contourf(VAR0,15);xlabel('Time(Hours)');ylabel('Azimuthal angle(deg.)');
set(gca,'YTickLabel','45|90 N|135|180 W|225|270 S|315|0 E')
axis on
grid off
figure;
plot(directionMatrix2,'o');
```

B.5 Log normal daily averaged total variance plots

```
Files=dir('Datafiler'); Folder='Datafiler\'; %The first 50 lines are
TotData=[];                                  %excactly the same as for
hmin=83; hmax=91;hint=2;n=(hmax-hmin)/hint; %the NetVar script.
numberOfDays=234;
for i = 3:numberOfDays+2;
    CombStr=strcat(Folder,Files(i).name);
    Data=LesDataWTD(CombStr);
    Data(:,2)=Data(:,2)+(i-3)*240000;
    FData=FilterAmbigHTheta(Data,hmax,hmin);
    FData(all(FData==0,2),:)=[];
    TotData=[TotData;FData];
end

PHI00=(TotData(:,8)/360)*2*pi;THETA00=(TotData(:,7)/360)*2*pi;
LOS00=(TotData(:,5));RANGE00=TotData(:,3);T0=TotData(:,2);
HEIGHT00=TotData(:,4);L=length(LOS00);
U=zeros(24*numberOfDays,n);V=zeros(24*numberOfDays,n);
VAR=zeros(24*numberOfDays,1);VAR1=zeros(24*numberOfDays,1);
t=1:1:24*numberOfDays; d=1:1:numberOfDays ;AVGVAR=zeros(numberOfDays,1);
T=zeros(L,1); X=zeros(L,1); Y=zeros(L,1); DELTALOS=zeros(L,1);
PHI0=zeros(L,1);THETA0=zeros(L,1);LOS0=zeros(L,1);RANGE0=zeros(L,1);
flag1=0;flag2=0;

for l = 1:n
    HH=find(HEIGHT00<=(hmin+hint*l) & HEIGHT00 >=((hmin-hint)+hint*l));
    PHI0(HH)=PHI00(HH);
    THETA0(HH)=THETA00(HH);
    LOS0(HH)=LOS00(HH);
    RANGE0(HH)=RANGE00(HH);
    T(HH)=T0(HH);
    for k = 1:24*numberOfDays
        BB=find(T<=(2+k)*10000 & T>(k-1)*10000 & T~=0);
        CC=find(T<=(k+1)*10000 & T>(k)*10000);
        if length(BB)<=1;
            flag1=flag1+1;
            continue
        end
        PHI=PHI0(BB);
        THETA=THETA0(BB);
        LOS=LOS0(BB);
        RANGE=RANGE0(BB);
        PHI1=PHI0(CC);
        THETA1=THETA0(CC);
        LOS1=LOS0(CC);
        RANGE1=RANGE0(CC);
        [fitresult, gof] = createSurfaceFit(PHI,THETA,LOS);
        U(k,l)=fitresult.U;
        V(k,l)=fitresult.V;
        for j = 1:length(CC);
            DELTALOS(CC(j))=LOS1(j)-(U(k,l)*sin(THETA1(j))*cos(PHI1(j))+...
            V(k,l)*sin(THETA1(j))*sin(PHI1(j)));
            X(CC(j))=sin(THETA1(j))*cos(PHI1(j))*RANGE1(j);
```

```
            Y(CC(j))=sin(THETA1(j))*sin(PHI1(j))*RANGE1(j);
        end
    end
    T=zeros(length(PHI00),1);
end                                 %Same as for NETVAR aswell

for k=1:24*numberOfDays
    BB=find(T0<=(2+k)*10000 & T0>=(k-1)*10000);
    if length(BB)<=1;
        flag2=flag2+1;
    end
    DELTALOS3=DELTALOS(BB);
    LOS3=LOS00(BB);
    VAR(k)=var(DELTALOS3);          %Gets total variance in pert.los velocity.
    VAR1(k)=var(LOS3);
end
VAR2=log(VAR);                          %Take log to be able to average.
for m = 1:numberOfDays                  %Average variance.
    AVGVAR(m)=mean(VAR2(1+(m-1)*24:24*m));
end
AVGVAR1=exp(AVGVAR);                %Take exponential to get averaged variance
figure; plot(t,VAR); xlim([0 24*numberOfDays]);
figure; hist(VAR);
figure; plot(d,AVGVAR1,'*-');ylim([50 260]);
```

B.6 Average monthly vector plots

```
VAR(isnan(VAR))=[];
l = length(VAR);

complexWindVector=zeros(l,1);
directionMatrixAngles=zeros(l,1);

%Makes the indecies in directionMatrix into radians, 0 to 2pi.
for i = 1:8
    indicies=find(directionMatrix2==i);
    directionMatrixAngles(indicies)=(pi/2)+(i-1)*(pi/4);
end
clear i;

%Makes a complex number for each hour to make it possible to average.
for j = 1:l
    complexWindVector(j)=VAR(j)*(cos(directionMatrixAngles(j))+...
    i*sin(directionMatrixAngles(j)));
end

%Averges 696 hours or 29 days for each itteration. Also getting the
%standard devitaion and standar error of the  x and y.
for k = 1:8
    monthlyMeanComplexNo(k)=mean(complexWindVector(1+(k-1)*696:k*696,1));
    standardDx1(k)=std(real(complexWindVector(1+(k-1)*696:k*696,1)));
    standardDy1(k)=std(imag(complexWindVector(1+(k-1)*696:k*696,1)));
    standardEx1(k)=(std(real(complexWindVector(1+(k-1)*696:k*696,1))))...
    /sqrt(696);
    standardEy1(k)=(std(imag(complexWindVector(1+(k-1)*696:k*696,1))))...
```

```
    /sqrt(696);

    x1(k)=mean(real(complexWindVector(1+(k-1)*696:k*696,1)));
    y1(k)=mean(imag(complexWindVector(1+(k-1)*696:k*696,1)));
end

%Plots the vectors with the standard error in x and y.
quiver(x1,y1,'b','linewidth',2);
hold on
quiver(x1+standardEx1,y1+standardEy1,'b:','linewidth',0.5);
quiver(x1-standardEx1,y1-standardEy1,'b:','linewidth',0.5);
quiver(x1+standardEx1,y1-standardEy1,'b:','linewidth',0.5);
quiver(x1-standardEx1,y1+standardEy1,'b:','linewidth',0.5);
```